NASA CR-54642

Cosmic, Inc. Report No. 106

FINAL REPORT

FURTHER DEVELOPMENT OF A CHARGED LIQUID COLLOID SOURCE FOR ELECTROSTATIC PROPULSION

by

D. Gignoux, H.F. Anton, J.J. Shea and R.M. Moriarty

prepared for

NATIONAL AERONAUTICS AND SPACE ADMINISTRATION

October 1965

CONTRACT NAS3-6268

Technical Management
NASA Lewis Research Center
Cleveland, Ohio
Electric Propulsion Office
John Ferrante

COSMIC, INC.
3206 Grace Street, N. W.
Washington, D. C. 20007

TABLE OF CONTENTS

SUMMARY

16161

A beam of charged liquid particles has been proposed for electrostatic thrustors. Experiments accomplished with a spinning nozzle in a vacuum, having its edge submitted to an intense electric field, resulted in operation for several hours with high beam currents and substantial thrust. Several propellants consisting of a solution of a salt in an organic solvent have been selected by a chemical analysis and tried successfully in the system. A performance mapping experiment has been accomplished. An analytical investigation has resulted in a theory which predicts performance parameters as a function of operating parameters. This theory checks a part of the data. It has been determined that further understanding of electrostatic spraying in vacuum will require knowledge of the influence of the residual atmosphere near the edge of the nozzle and in the vacuum chamber.

Author

LIST OF FIGURES

LIST OF SYMBOLS

Symbol	Definition	Dimension
a	characteristic size of droplet	L
b	radius of quadrupole rails	L
d	radius of quadrupole	L
e_o	normalized electric field at source	1
f	frequency	$1/T$
f_n, g_n	dimensionless functions defined by space-charge flow	1
h	film thickness	L
j	normalized current density	1
l	characteristic length of electrode system	L
m	mass of droplet	M
$\dot{m}$	mass flow rate	M/T
q	charge of droplet	Q
r	radius of nozzle	L
s	electrode separation in parallel plane geometry	L
v	exhaust velocity of droplet	L/T
A	emissive area	L^2
B	dimensionless constant in expression for space-charge limit	1
$C_{1,3}$	dimensionless constants in expressions for charge-to-mass ratio	1
D	dimensionless constant in expression for film thickness	1
E	electric field	ML/T^2Q
F	thrust of beam	ML/T^2
G	coefficient in Mathieu equation	1
H	dimensionless function determined by space-charge flow	1
J	current density of beam	Q/L^2T
K	dimensionless function determined by space-charge flow	1
$K_{1,2,3,4}$	dimensionless constants in expressions for charge-to-mass ratio	1
L	distance between nozzle and extractor electrode	L
P	power of beam	ML^2/T^2
T	temperature	1
V	voltage	ML^2/T^2Q

Symbol	Definition	Dimension
γ	surface tension of propellant	M/T^2
ϵ	capacitivity	T^2Q^2/ML^3
λ	dimensionless parameter depending on controllable elements	1
μ	dimensionless parameter depending on controllable elements	1
ν	kinematic viscosity	L^2/T
ρ	resistivity of propellant	ML^3/TQ^2
ρ_m	mass density of propellant	M/L^3
σ	conductivity of propellant	TQ^2/ML^3
τ	characteristic time available for charging droplet	T
ω	angular velocity of nozzle	$1/T$
Γ	dimensionless parameter depending on controllable elements	1

1. INTRODUCTION

The past 12 months have seen spectacular achievements in space. Although dwarfed by the performance of the first sustained space flight by human beings, the tests of electric propulsion devices which took place are no less significant. It has been proven that electric engines can perform in space, that the beam of an ion engine can be neutralized and that the performance of such an engine is that which was anticipated. It is now time to assess the significance of the electric propulsion effort which took place during the past five years, and also examine the problems and limitations which have been encountered or are predictable. This leads us to examine objectively the potential of all the thrustor concepts and weigh the possible advantages of the colloid beams to be discussed in this report versus the characteristics of the better known ion engines.

In an electrostatic thrustor, we are faced with the problem of the choice of the electrical particle to be accelerated. Cesium or mercury ions have been used in the thrustors currently under test. The advantages of using particles with a much lower charge-to-mass ratio than ions are twofold: first, this enables a higher power efficiency than is attainable with ion thrustors especially in the low specific impulse range. Secondly, the same thrust may be obtained with a smaller emissive surface when the particles have a higher mass. Thus, a thrustor utilizing a charged colloid beam instead of an ion beam will have a smaller cross-section and, given an adequate method of producing the charged colloid, will have lower weight. Naturally, in order to obtain the same thrust a higher acceleration voltage will be required. This means that the engine will accelerate particles over a longer distance and will utilize a higher voltage. The handling of the power at very high voltages is a delicate matter, especially in vacuum. For this reason, design limitations have to be introduced; for instance, 100,000 volts is the limit up to which electrode and insulator designs are basically the same as those used in the voltages of ion engines (up to 5,000 volts). Between 100,000 and 500,000 volts, specially designed equipments have to be used, for instance, voltage dividers, shields, etc. Above 500,000 volts, new considerations complicate the design and render the system substantially heavier and more costly. Therefore, in the design of colloid thrustors one should try to remain below the limit of 100,000 volts if possible and at any case, not exceed 500,000 volts. The above consideration enables one to determine what the charge-to-mass ratio of the particles should be. In order to compete with the ion engine at low specific impulse, the charge-to-mass ratio must vary between 3,000 and 10,000 coulombs/kilogram.

We have thus far implied "a beam" where all particles have the same charge-to-mass ratio. In general this is not the case and an ion beam will consist of ions singly charged, doubly charged, and also a certain amount of neutrals. In a colloid engine, the situation is even more complicated as, in addition to the presence of neutrals, the beam itself consists of particles having charge-to-mass ratios with an unknown distribution, resulting in a reduction in efficiency.

We have therefore defined above the main performance parameters required from a charge liquid colloid source so that its application in an electric thrustor can be envisaged: an average charge-to-mass ratio of a particle between 3,000 and 10,000 coulombs/kilogram, a few neutrals in the beam and a distribution of the charge-to-mass ratio sufficiently narrow to make possible a thrustor with a high efficiency. To these requirements we must add that the source must be capable of generating colloids in sufficient quantity to obtain a substantial current, a substantial thrust and be capable of operating over a long period of time.

The method of generation of colloids which has been the subject of the largest effort to date is the vapor condensation method utilized in the NASA in-house program (Reference 1). This effort has demonstrated that beams of charged particles could be obtained in the right range of charge-to-mass ratio. The other method which has been suggested by the writers of this report consists in electrostatic atomization and charging by means of spraying of the liquid in an intense electric field. The device used to this end is shown in Figure 1. A liquid is fed into the center of a spinning, hollow, conical nozzle and by virtue of the centrifugal force forms a thin film on the inside of the nozzle. A ring (extractor) is disposed slightly beyond the edge of the nozzle and between the nozzle and the ring there exists a difference of potential of the order of 50,000 to 100,000 volts. As the film of liquid comes to the edge, it is atomized and charged in the region immediately surrounding the nozzle and in which there exists an intense electric field.

This method of obtaining a charged colloid is in principle no different from the method which consists of feeding the liquid to the top of a hollow needle submitted to an intense electric field (Reference 5). Experiments accomplished by the latter method have had the merit of proving the possibility of generating a colloid beam in the charge-to-mass ratio range of 500 to 2,000 coulombs/kilogram. However, the mass flows that have been used are so small as to render the device impractical unless a very large array of needles were used. The spinning nozzle has been analyzed in Reference 2 and further described in References 3 and 4. Considerable progress has

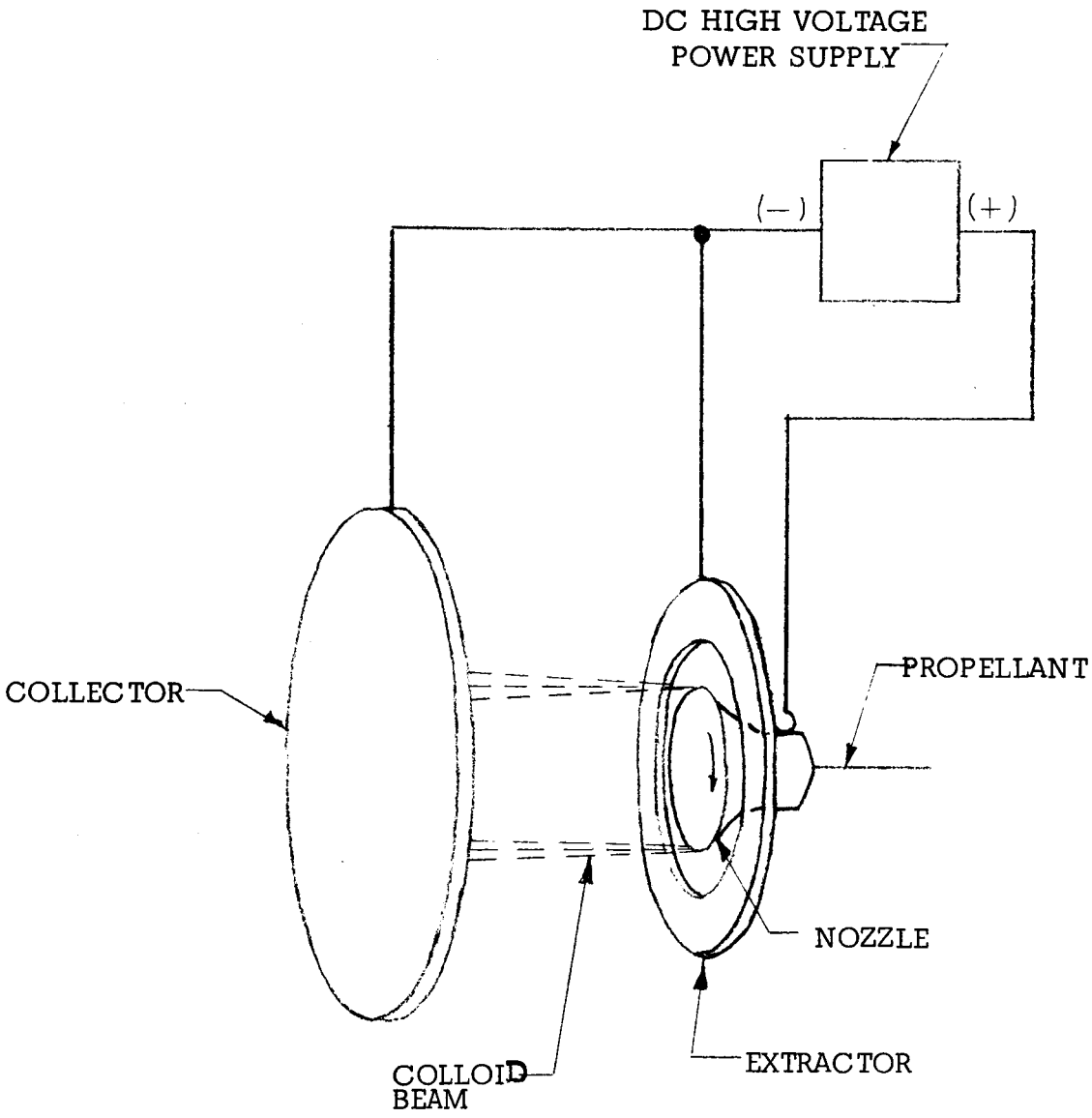

Figure 1. Principle of Operation of Spinning Nozzle Charged Liquid Colloid Source.

been made, and high thrust and currents have been achieved. In this report we shall explain the operation of the system, the instrumentation that is used with it, present a theory, compare it with the data, report on research accomplished on propellants, and finally present the results of a performance mapping experiment accomplished by varying several of the parameters.

2. DESCRIPTION OF THE EXPERIMENT

The experimental research program undertaken has consisted in the improvement of a test setup and instrumentation already existing under a previous program. A number of tests were then accomplished with the equipment. In this section we shall describe the equipment used.

2.1 General Description

Figure 2 shows an overall view of the system, the heart of which is the vacuum chamber. The chamber itself consists of a glass cylinder 20 inches long by 23 inches in diameter with metal end plates at both ends. The glass cylinder is surrounded by a plexiglass cylinder in order to protect the operators against the danger of implosion, while permitting full visibility. One of the end plates is fixed, and on it is mounted the nozzle, its drive and the high voltage bushing with the propellant feed tube. The other end plate is moveable, mounted on hinges and supports the collector. The ring extractor is supported by the glass cylinder. The pumps will be described separately.

We shall now describe in detail each component of the equipment.

2.2 High Voltage Power Source

The power supply is an electrostatic generator of the constant oblique field type described in Reference 6. It consists of four rotors 5 inches in diameter, and is capable of a maximum current of 2 milliampere and a maximum voltage of 100,000 volts. Its internal capacitance is negligible and it can therefore be utilized without protection. Sometimes during a test an operator received an electric shock at a voltage of around 80,000 volts. The only effect was an unpleasant sensation. A voltage multiplier, transformer-rectifier type of power supply with an output of up to 50 kilovolts and a current up to 5 milliampere was also used in some tests. With the latter power supply, the danger of electric shock made it necessary to take the usual safety measures. These served to protect the personnel more than the equipment. In particular, during a test a discharge occurred in the vacuum chamber and serious damage was done to one of the instruments inside the chamber: the electrobalance which will be described later.

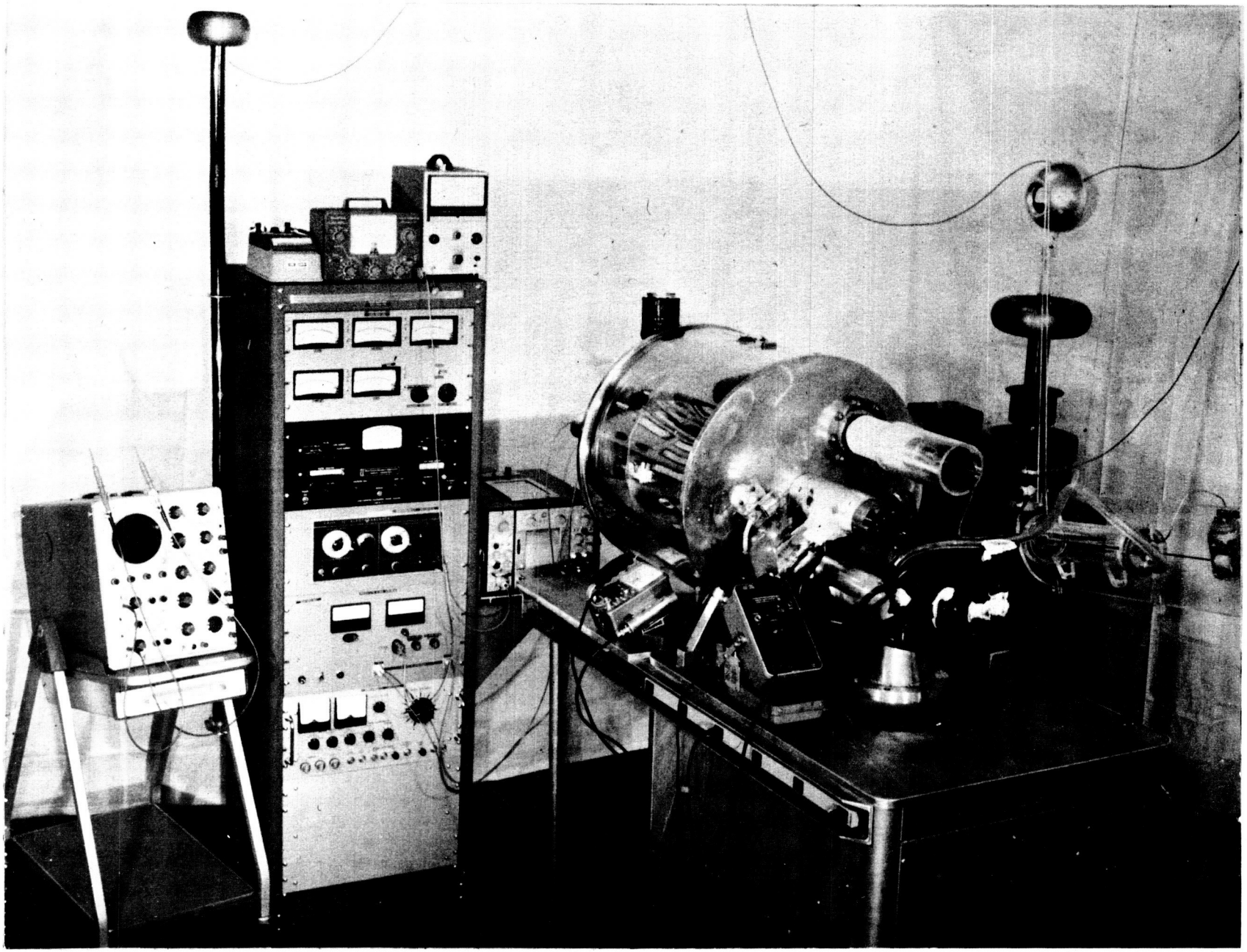

Figure 2. Overall View of Testing Facility

2.3 Propellant Feed Systems

The propellant feed system is shown on Figure 3. Its design requires some explanation. In the propellant feed system used in the previous program (Reference 4), gas bubbles would sometimes be present. To correct this defect, the system is placed inside an auxilliary vacuum chamber. The piston is driven by means of several synchronous motors resulting in the following mass flows for a propellant having a density of 1,000 kilograms/cubic meter: 0.25, 0.5, 1.5, 3, 7.5, 15, and 30 x 10^{-6} kilograms/second.

The propellant system, which is shown in Figure 3, has the metering tube installed in an auxilliary vacuum chamber with the propellant stored in a vacuum tight reservoir that has been soldered into the system. Thus, the propellant is stored and transferred under vacuum. The loading of the piston is then accomplished as follows: the piston is withdrawn from the metering tube and the reservoir containing the liquid is then turned up so that the propellant flows by gravity into the tube. Once the tube is full, the reservoir is then turned right side up, interrupting the flow of propellant. The auxilliary vacuum chamber, which contains the propellant feed system, is normally evacuated by means of a flexible tube connected to the elbow of the main vacuum chamber. However, since the auxilliary vacuum chamber is not pumped directly, its pressure may be several orders of magnitude higher than that of the main vacuum chamber. For this reason, glow discharges may occur. In order to avoid this, the connection between the elbow and the auxilliary vacuum chamber is closed while a test is being run. This and other difficulties are of course due to the fact that the propellant feed system is entirely at the high voltage. To prevent discharges along the insulator or through the atmosphere, the system is mounted on an insulating board which was first supported on an insulating frame. It was found that suspending the assembly from the ceiling by means of nylon ropes was the most satisfactory solution.

2.4 The High Speed Drive

The high speed drive has been described previously (Reference 4). It consists essentially of a thin-walled, closed cylinder attached to the vacuum chamber with the vacuum on the inside and the air on the outside. Magnetic coupling enables a magnet on the outside, rotated by means of an electric motor, to drive an iron rotor on the inside. In a previous program, overheating of the unit prevented continuous operation at high speeds. Forced air cooling was added, making continuous operation at speeds up to 15,000 rpm possible. This drive appears to be the highest speed vacuum drive, capable of a four-inch-pound torque, in existence today.

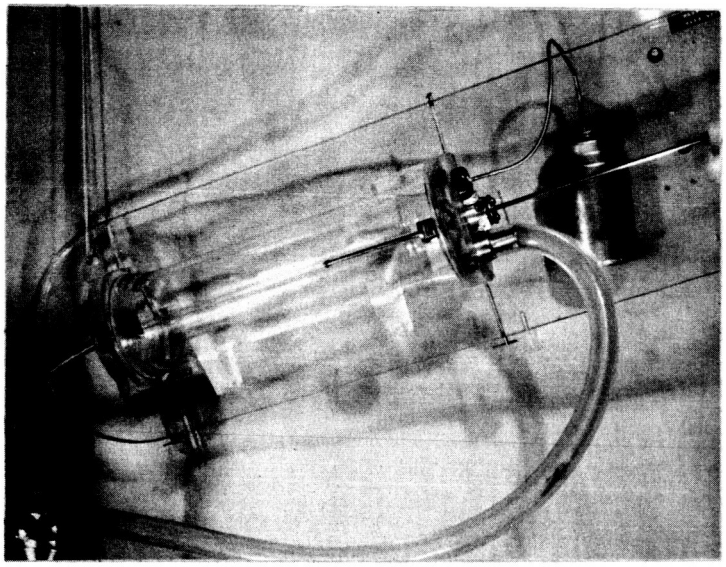

Figure 3. Propellant Feed System.

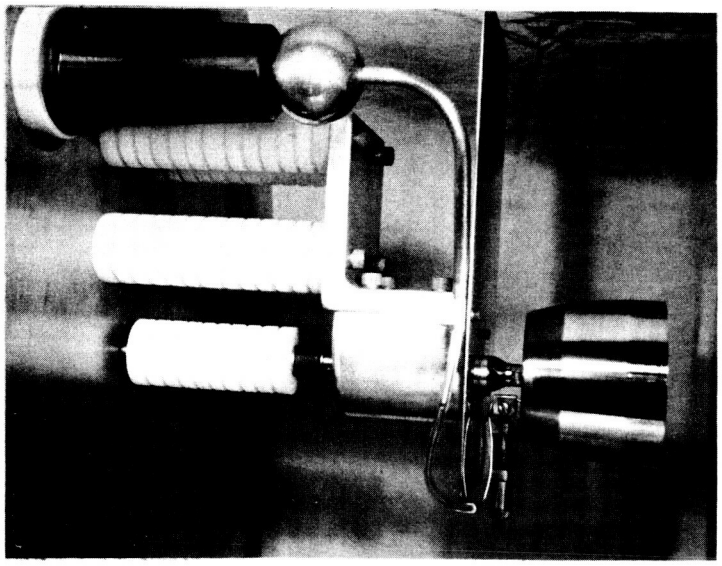

Figure 4. Nozzle and Nozzle Support System, High Voltage Feedthru and Propellant Feed Tube Adjusting Mechanism.

2.5 The Nozzle and Its Support

The nozzle is mounted on a drive assembly that is attached to the back plate by means of four insulated stand-offs (Figure 4). The difficulty of attaining a high speed in a vacuum chamber is here augmented by the fact that the nozzle and therefore its entire support assembly must be at the high voltage. This requires the use of a long coupling. The nozzle can be seen in Figures 5 and 6. It is machined from a solid piece of metal and consists essentially of two cavities that are connected by means of a series of holes parallel to the axis. The propellant is delivered to the rear cavity, and then flows through the holes into the front cavity. Some difficulties were encountered in obtaining a steady mass flow of propellant especially at the very low mass flow rates. The effect was a drop by drop propellant delivery instead of a uniform one. A device has been made which permits adjustment of the end of the propellant delivery tube so as to have the end of the tube extremely close and parallel to the surface of the back cavity of the nozzle. The wiping action that results eliminates any chance of drops forming. This device is shown in Figure 4.

2.6 The Extractors

At the beginning of the program, the extractor was mounted on the collector by means of insulated supports. The advantage of this disposition was that it was then possible to move the extractor from the outside of the vacuum chamber during a test. However, the extractor supports became coated with propellant during the "voltage-off" periods. This resulted in electrical discharges from the supports when the voltage was again turned on. The disposition which has been finally adopted consists of supporting the extractor directly on the glass vacuum chamber by means of three legs. These legs are spring loaded so that they press on the glass with an even pressure before and after pumping of the vacuum chamber.

2.7 The Collector

The collector is a flat metal plate and can be seen in Figure 7. It intercepts the beam and is provided with two windows behind which are mounted two instruments described in another chapter: the mass filter and the thrust and mass flow measuring devices. The collector is mounted on four rails so that it can be moved from outside the vacuum chamber. Provision is made for the collector to be cooled by liquid nitrogen. It was felt that the cold collector would act as a cryogenic pump and help keep a low pressure in the region of the beam. However, it was found that in the tests that were run with liquid nitrogen cooling that discharges were initiated by the frozen propellant that accumulated on the collector.

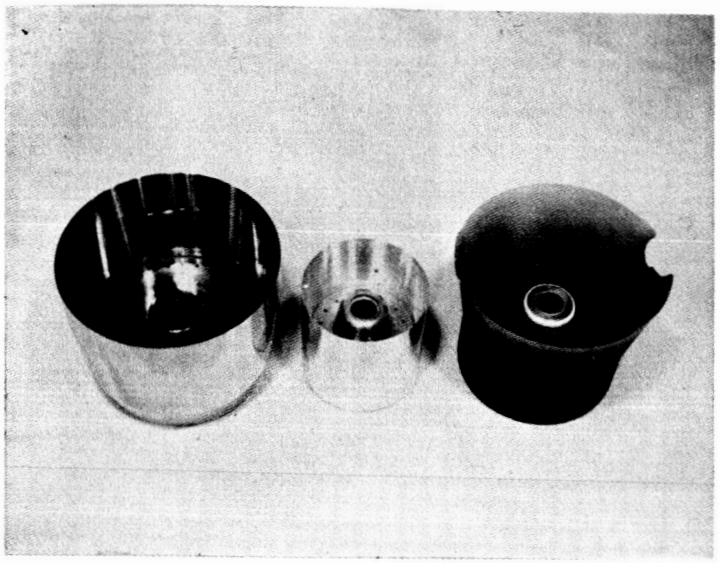

Figure 5. Three Nozzles. The Nozzle on the Right is an Epoxy Nozzle Which was Damaged by Heat.

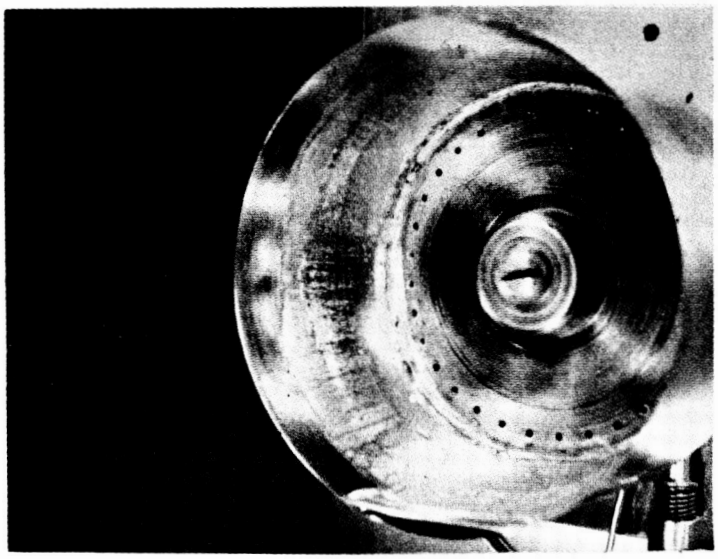

Figure 6. 10° Nozzle Closeup with Liquid Metal.

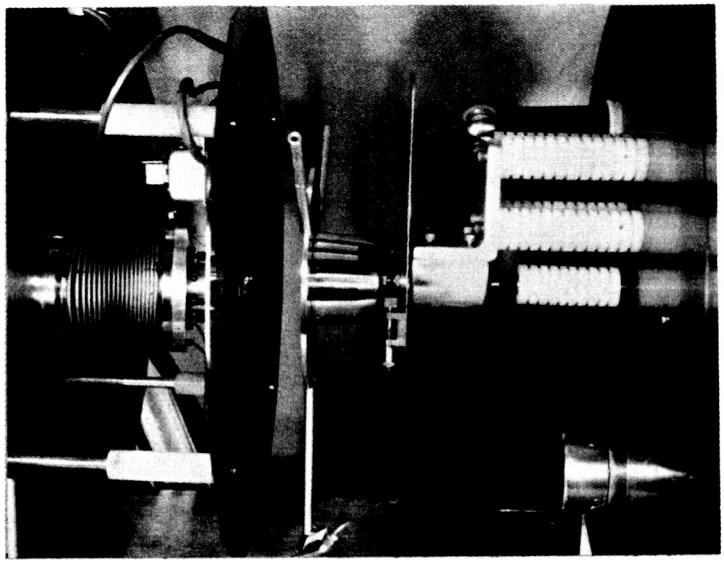

Figure 7. Inside View of Chamber.

2.8 High Vacuum Pumping System

Three different pumping systems have been used:

1) In the initial phases of the program, the vacuum chamber was connected by means of an elbow to a high vacuum valve and then, via a second elbow, to the oil diffusion pump. A water cooled baffle and a liquid nitrogen cold trap were positioned above the pump. The test data shown in Figures 14 and 15 was obtained with this system.

2) A liquid nitrogen cooled coil was later placed between the collector and the hinged end plate of the vacuum chamber. No substantial improvement in system performance was experienced as a result of the modification. The liquid nitrogen coil was then soldered to the back of the collector plate, the ends of the coil passing through insulating bushings so as not to interfere with current measurements. A vacuum could then be maintained in the low 10^{-6} range throughout a test, however, solid propellant deposits on the collector initiated discharges as described in the preceding section.

3) In a subsequent modification, the high vacuum valve was removed and the pump attached directly below the elbow without a baffle. A liquid nitrogen trap, shown in Figure 8, was then made and centered in the elbow. The resulting pumping speed was subsequently higher and this configuration was used for all performance mapping experiments.

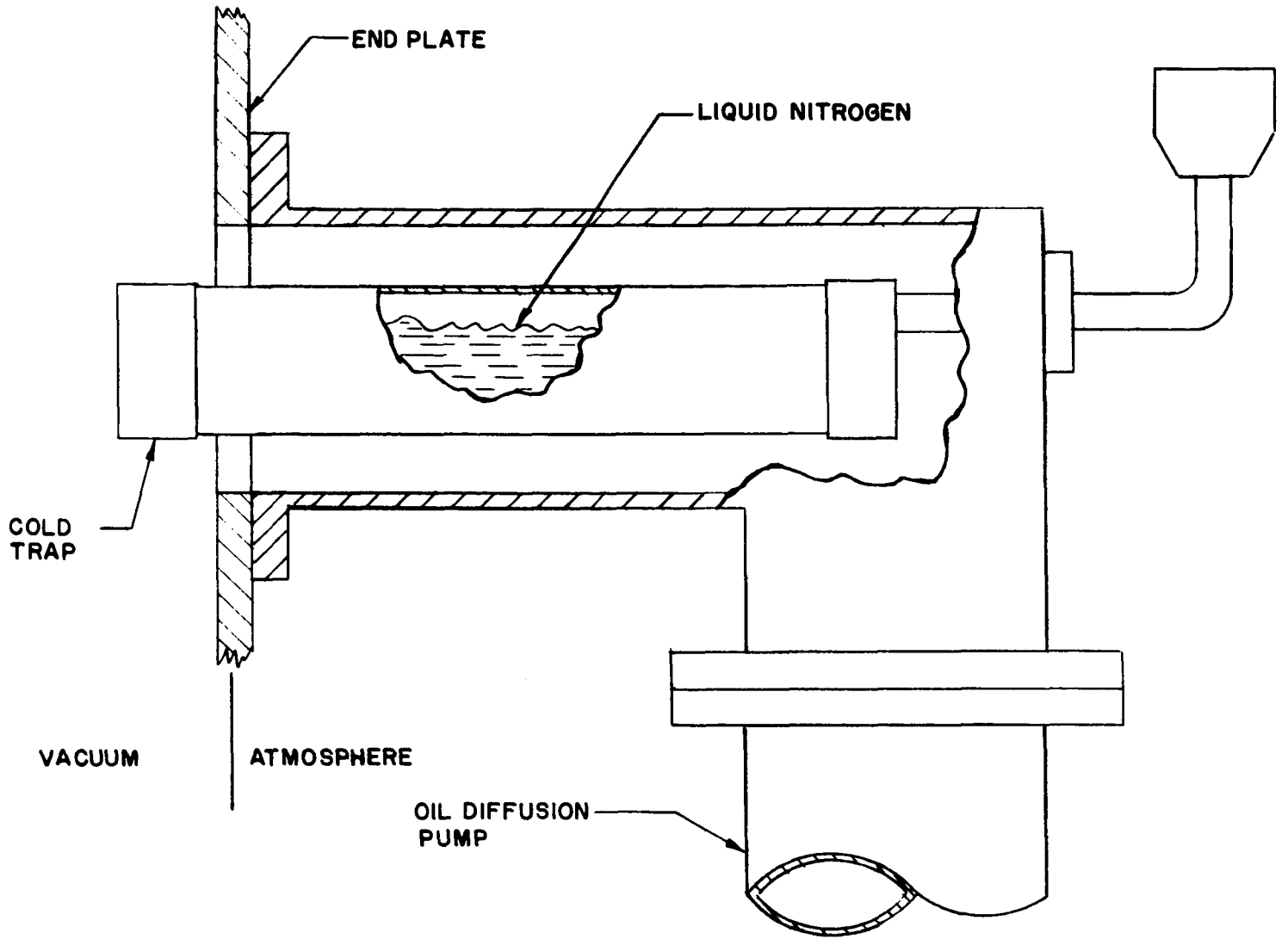

Figure 8. Sketch of Liquid Nitrogen Cold Trap and Oil Diffusion Pump.

3. INSTRUMENTATION

3.1 General

A schematic of the instrumentation is shown in Figure 10. The instrumentation provides for the measurement of thrust, mass flow, voltage and the relevant currents. Two instruments deserve special description: the thrust measuring device and the mass filter.

3.2 Thrust Measuring Device

Behind one of the two windows in the collector is mounted a thin titanium plate which intercepts the beam that passes through the window. This plate is utilized to measure the thrust as well as the mass flow of the propellant intercepted. This plate, referred to as the target, is mounted on a pivot point as shown in Figure 9. The thrust on the plate, which is a horizontal force, and the weight due to the accumulation of propellant on the target result in moments in the same direction with respect to the pivot. These moments are compensated for by a microbalance movement. The indication of the microbalance is continuously recorded. The thrust is obtained by the difference in the indication of the microbalance between the measurements with "voltage on" and with "voltage off". The mass accumulation can be estimated two ways. First, by the difference in weight of the plate between the indication of the balance at the two "voltage off" periods, between the end and the beginning of a test, and by the slope of the curve of microbalance measurement as a function of time during a test.

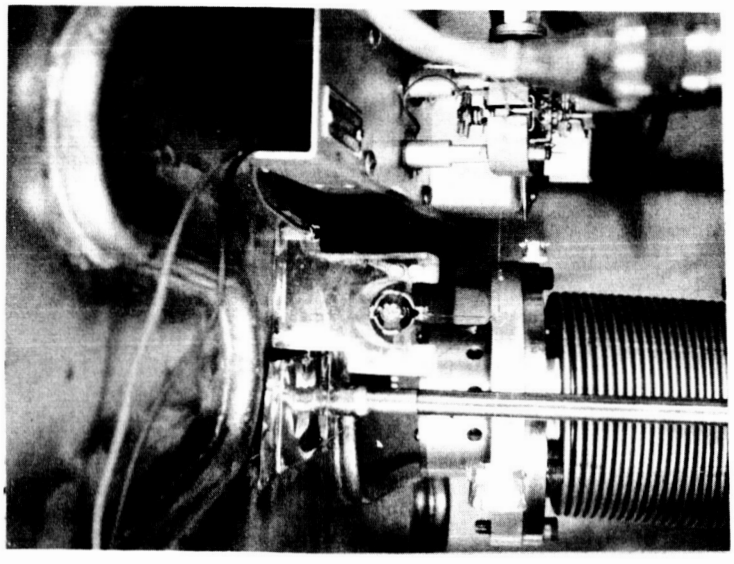

Figure 9. Thrust and Mass Flow Target, Electro Balance - The Below in the Background is Part of the Quadrupole.

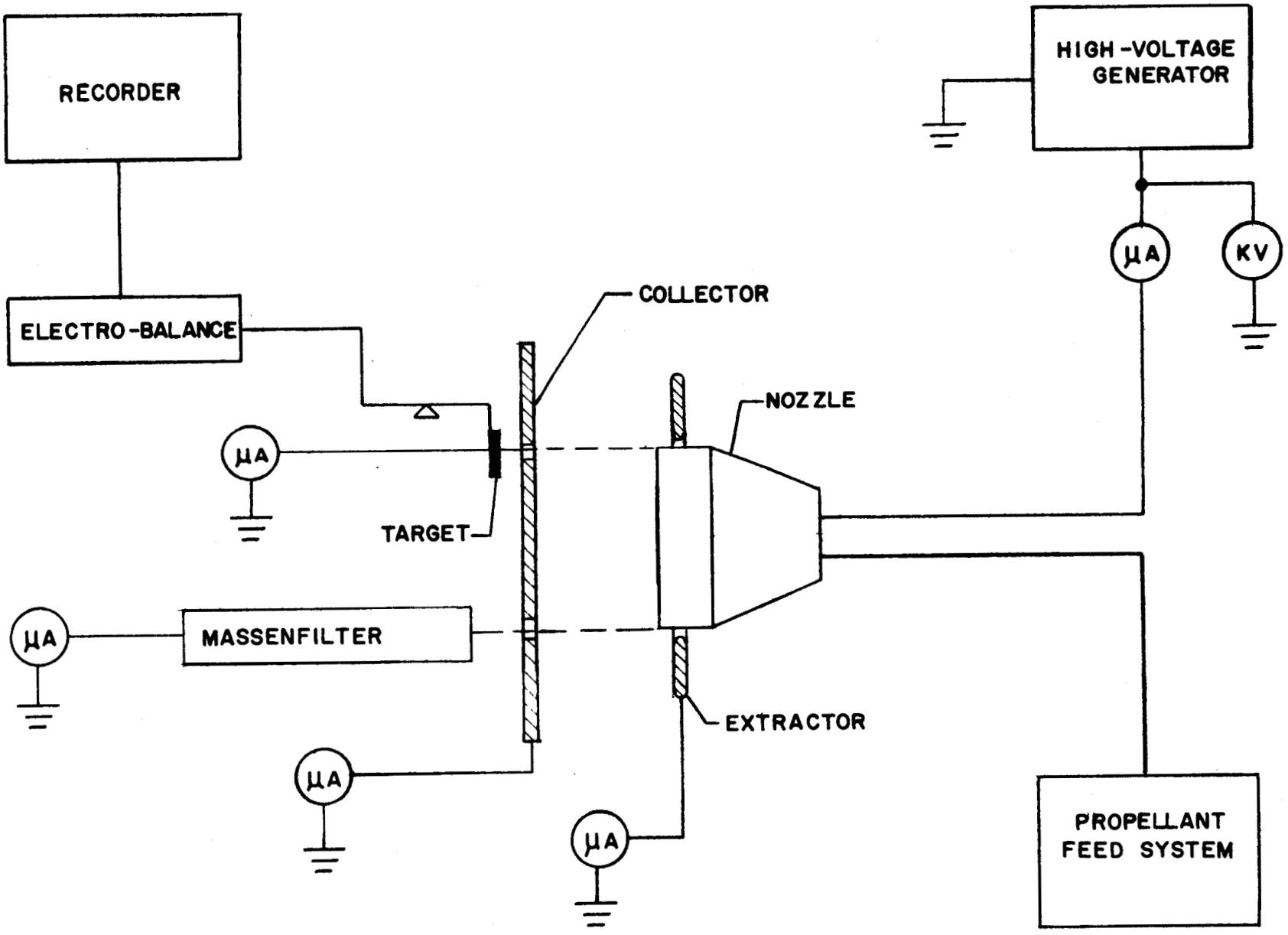

Figure 10. Schematic of Instrumentation

3.3 Mass Filter

To obtain a distribution of particle charge-to-mass ratio, it would appear that the easiest method would be to utilize a magnetic beam separator. However, in view of the large mass of some of the particles, this would entail extremely powerful magnets. A much more elegant method of obtaining a distribution of charge-to-mass ratio consists in using purely electric fields. It is well known that two particles of different charge-to-mass ratios will follow the same trajectory in a static electric field, but not with the same velocity. It appears therefore conceivable that a time varying, non-uniform electric field may be used to separate particles according to their charge-to-mass ratio. This is possible, in particular, with a field having the following components in an x, y, z, system of orthogonal coordinates:

$$E_x = - (U_o + U_1 \cos 2 \pi f t) \frac{x}{d^2}$$

$$E_y = (U_o + U_1 \cos 2 \pi f t) \frac{y}{d^2}$$

$$E_z = 0$$

The notations used above have a meaning which will become clear in a later portion of this report. We will assume that the particle having a charge-to-mass ratio, q/m, is initially moving along the z axis, having been accelerated by a difference of potential V.

The field given above can be derived from the potential function

$$U(x, y, z, t) = 1/2 \, (U_o + U_1 \cos 2 \pi f t) \frac{y^2 - x^2}{d^2}$$

which can be obtained by applying the potentials $\pm 1/2 \, (U_o + U_1 \cos 2 \pi f t)$ on the hyperbolic cylinders $y^2 - x^2 = \pm d^2$. In practice, such hyperbolic cylinders are replaced by circular cylinders having a radius b = 1.16 d, as shown on the following figure:

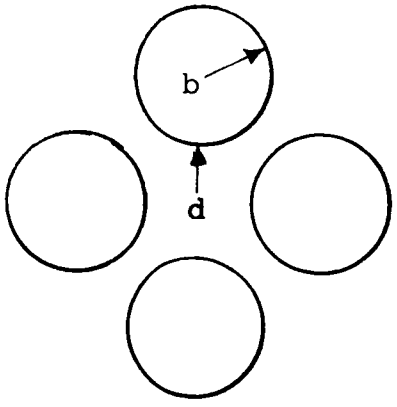

This b/d ratio is the one which gives the best approximation of the hyperbolic field, according to Dayton (Reference 7). With respect to time, the equations of motion become:

$$\ddot{x} + (U_o + U_1 \cos 2\pi f t)\frac{x}{d^2}\frac{q}{m} = 0$$

$$\ddot{y} - (U_o + U_1 \cos 2\pi f t)\frac{y}{d^2}\frac{q}{m} = 0$$

$$\ddot{z} = 0$$

The third equation can be immediately integrated to yield:

$$z = (2\frac{q}{m}V)^{1/2} t$$

whereas the first two can be transformed into known forms by the transformation:

$$T = \pi f t$$

$$G = U_1 q (2d^2 m \pi^2 f^2)^{-1}$$

Thus, the equations of motion become:

$$x + G(2\frac{U_o}{U_1} + 2 \cos 2T)\, x = 0$$

$$y - G(2\frac{U_o}{U_1} + 2 \cos 2T)\, y = 0$$

which are the equations first encountered by Mathieu in a study of the vibration modes of elliptical membranes (Reference 8). Solutions of these equations are found in McLachlan (Reference 9).

Depending on the values of G and of U_1, the trajectories of the particles become stable or unstable as shown on the following diagram:

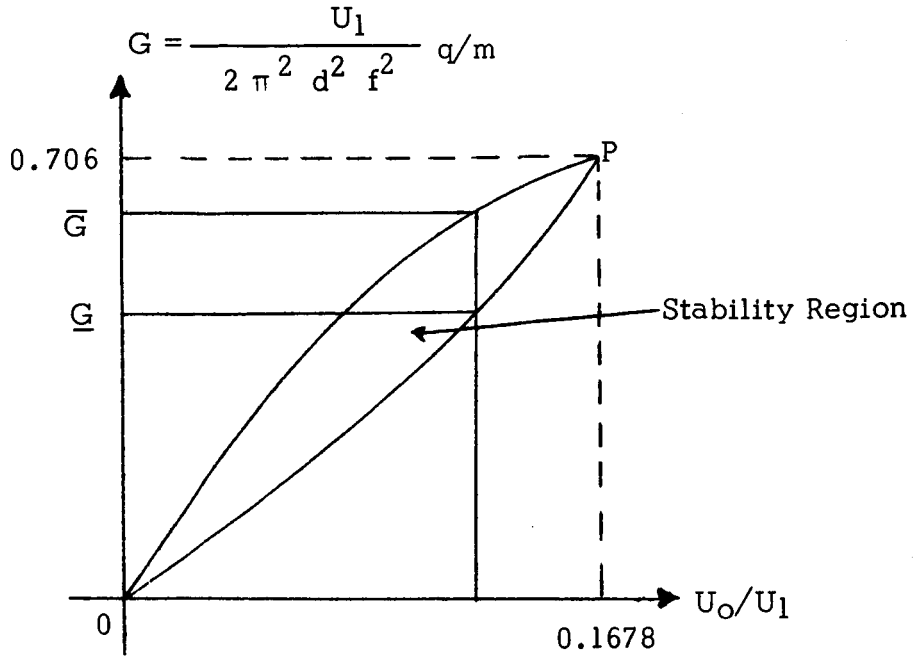

It is therefore shown, that for a fixed value of $\frac{U_o}{U_1}$ all particles having a q/m such that $\underline{G} < G < \bar{G}$ will yield stable trajectories and furthermore, will be the only ones to do so.

The resolution $R = \frac{q/m}{\Delta q/m}$ can then be calculated by:

$$R = \frac{\bar{G} + \underline{G}}{2(\bar{G} - \underline{G})}$$

Quadrupole Mass Filters are often used near the corner of the stability region (close to point P) and therefore $1/2(\bar{G} + \underline{G})$ is approximated by 0.706 and the resolution is obtained from the first terms of the development of $\bar{G}$ and $\underline{G}$ around P:

$$R = \frac{0.75}{1 - \frac{U_o}{U_1 \times 0.1678}}$$

As will be shown later, with colloid beams it is often preferable to operate with relatively low values of R. Therefore, the approximation we shall take for G is:

$$G \simeq \frac{U_o}{U_1 \times 0.1678} \times 0.706$$

which gives:

$$q/m = (13.93 \frac{d^2 f^2}{U_1}) \times (\frac{U_o}{U_1 \times 0.1678})$$

The value of q/m is given by the product of these two expressions. The first is the expression given by Paul (References 10 and 11). The second is a corrective factor which could also be written $1 - \frac{0.75}{R}$ and should be used at low resolutions. Values of the corrective factor and those of $\frac{U_o}{U_1}$ as a function of R are given below:

R =	1	2	3	4	5	10	50
$\frac{U_o}{U_1 \times 0.1678}$	.25	.625	.75	.8125	.85	.925	.985
$\frac{U_o}{U_1}$	.042	.105	.126	.1363	.142	.1552	.1653

The discussion above has referred to an ideal mass filter, i.e., one which is infinitely long and in which the particle has a low radial kinetic energy $1/2(\dot{x}_o^2 + \dot{y}_o^2)$ at the aperture as compared to the radial potential energy due to the quadrupole field:

$$\frac{1}{2} \frac{q}{m} (U_o + U_1)$$

To utilize the mass filter, we must find the conditions for which the equations above can apply, unfortunately, this has only been done for particles of charge-to-mass ratios 10^3 times higher and for accelerating voltages 10^2 times lower than those pertaining to colloids.

It is specifically recommended by Paul when using the device to separate isotopes (Reference 11, page 153), that the number of oscillations undergone by a particle in the quadrupole, N, be greater than $3.5\sqrt{R}$. This number is as follows:

$$N = 0.19\frac{L}{d}\left(\frac{U_1}{V}\right)^{1/2}$$

Thus, for R = 5 at least 7 oscillations should be undergone by the particles. This imposes the condition that L/d be at least 200.

It must be pointed out that the above recommendation for the number of oscillations, in addition to other operating criteria not described here, i.e., the size of the aperture and the angle of the beam with respect to the axis, have all been established with very different operating conditions than encountered in this study.

The quadrupole constructed here consists of four rods 1/8 inch in diameter and 16 inches long. The aperture is .090 inch in diameter. The entire assembly is attached to the vacuum chamber by means of a bellows, as can be seen in Figure 7. The adjusting screws make it possible to align the quadrupole with the beam. This is accomplished by orienting the quadrupole so as to obtain a maximum current on the quadrupole target in the absence of any rail voltage.

A view of the open quadrupole can be seen in Figure 11.

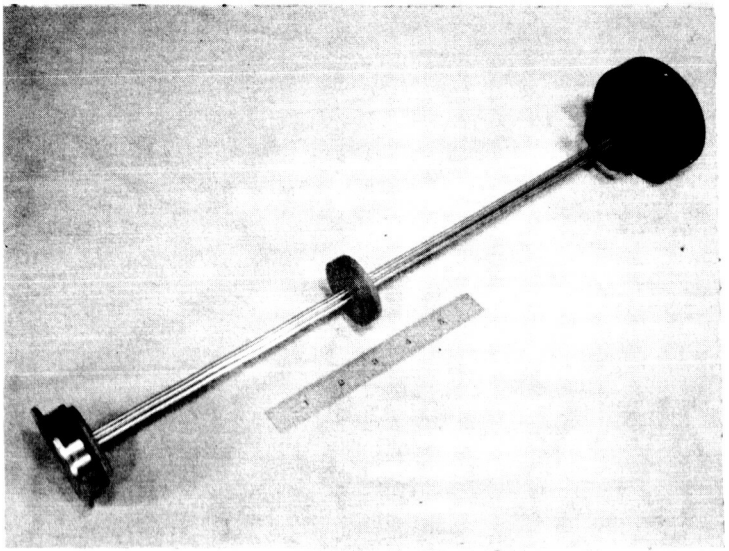

Figure 11. Quadrupole Mass Filter Rails.

The quadrupole mass spectrometer power supply is as shown in Figure 12. It consists of a high gain differential, audio/RF amplifier and a regulated DC power supply. Precision servo loops are used to control AC amplitude, AC amplitude balance and DC/AC ratio. A detailed description of the circuit follows.

V_1 (A & B) form a phase inverting input stage to develop push-pull signals from the single-ended input. In addition to providing balanced, 180° related signals this stage is adjustable in gain over a wide range, since cathode currents are supplied from constant current sources (Q_1 and Q_2) and cathode-to-cathode resistance is made variable. This variation (the CK-1114 combined lamp and light-dependent resistor) is under the control of the servo system that is concerned with maintaining output amplitude constant (AGC).

Amplification is then through similar further amplifiers except that the gain through one channel is dependent upon the condition of another CK-1114 lamp and light-dependent resistor. This device is controlled by the servo loop which maintains amplitude balance between the two AC signals to the quadrupole rails.

The output amplifiers are worthy of some comment. Each is essentially an operational amplifier comprising, for example, Q_7, Q_5, V_4 and V_6. Q_5 is a constant source tending to drive the grid of V_4 negative, the current from which is balanced by an equal current through Q_7 from the 500 KΩ feedback resistor. Signal currents, then, from V_2 (V_3 in the other channel) cause equal but opposite currents to flow in the feedback resistor. Thus, the output voltage is a faithful representation of the signal from V_2. V_6 and V_4 act during opposite half-cycles of the signal to charge and discharge the load capacitance respectively.

Output amplitude is sampled by amplifier A_1, a Philbrick P-45 wide band operational amplifier. The output of A_1 is peak rectified and used to control the current flow through Q_9 and Q_{10}. Q_9 and Q_{11} control the voltage of the DC power supply so that it is always a fixed fraction of the AC voltage. The particular fraction is determined by the setting of the DC/AC ratio control, a 10-turn precision potentiometer, the range of which is 0.1 to 0.2. Q_{10} develops a voltage at the emitter which is precisely proportional to the peak AC voltage. Amplifier A_2 compares this voltage with that of a reference source, and acting on the overall gain of the amplifier, serves to establish the correct operating level. This level is determined by the setting of the amplitude control which is another 10-turn precision potentiometer.

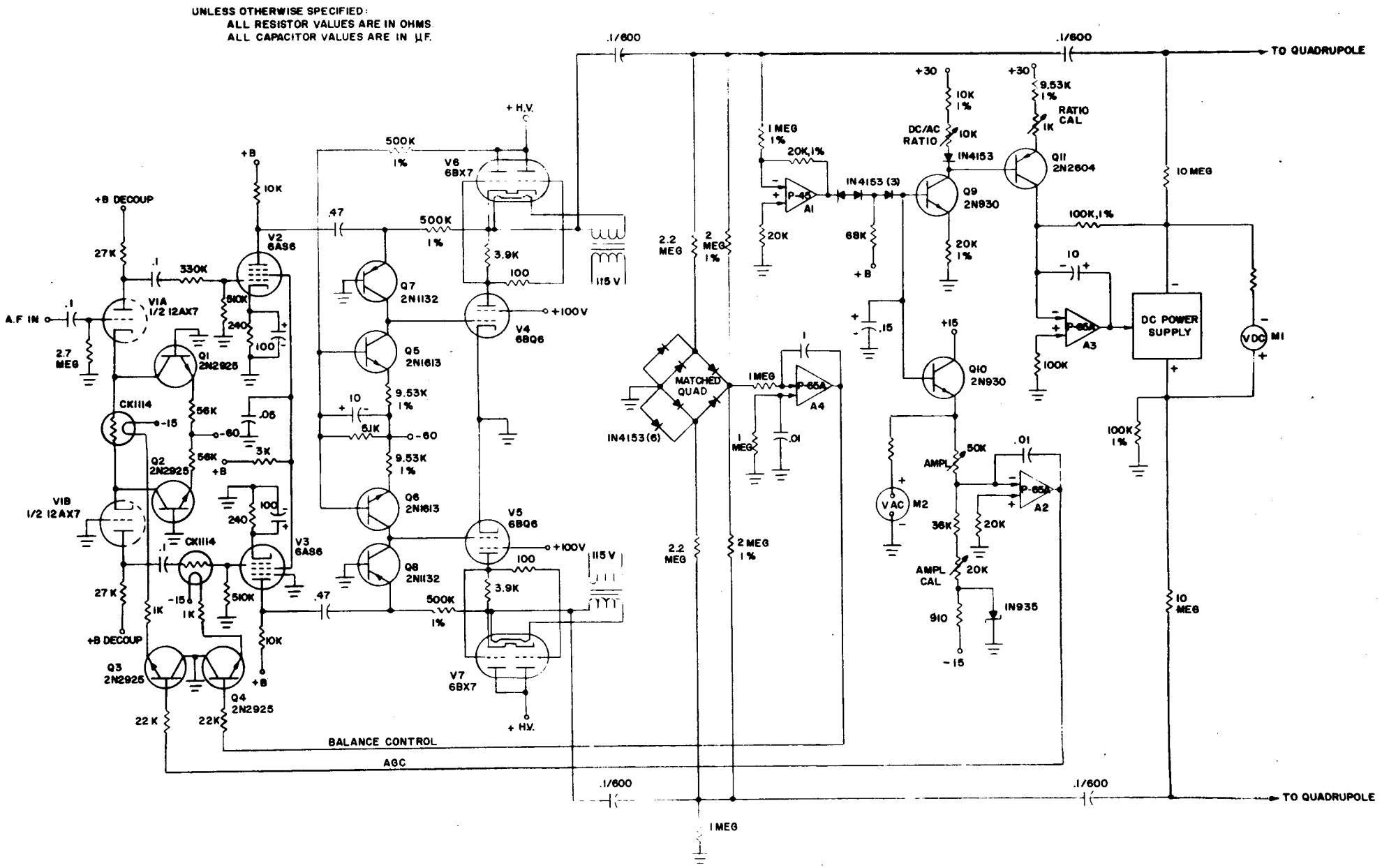

Figure 12. Schematic of Mass Filter Controls.

Amplitude balance is maintained by another servo loop comprising a phase detector and amplifier A_4. Output from the switched bridge of diodes (the phase detector) is non-zero if an imbalance exists between the amplitudes of the AC signals. Amplifier A_4 integrates any such error signal and controls the gain of one channel of the amplifier in such a way as to restore balance between the signals.

Metering of the DC and AC voltages is accomplished as shown. The total DC voltage is measured directly by M_1 which has an appropriate multiplier resistor. AC voltage is measured indirectly by monitoring the DC voltage at the emitter of Q_{10} (which is at all times proportional to the AC amplitude).

4. CHEMICAL INVESTIGATIONS OF PROPELLANTS

4.1 General

An investigation has been carried out dealing with solutions of polar solutes dissolved in non-volatile, high-molecular weight organic solvents. The object of the study was to find a solution possessing optimal properties required of a propellant for colloidal propulsion. Among these properties are:

(a) low vapor pressure
(b) low surface tension
(c) low resistivity
(d) chemical stability
(e) favorable viscosity

4.2 General Discussion of Solvents

Numerous organic solvents are available which possess the desired low vapor pressure. Solutions using as solvents polyhydroxy alkanes, esters of phthalic acid, phosporic acid and polyunsaturated straight chain alkanes have been studied.

The solvolysing power of an organic solvent towards polar crystalline substances depends largely upon specific electrostatic solvation forces such as dipole-dipole, ion-dipole, dipole-induced dipole, and hydrogen bonds. The limiting factor in the selection of a solvent is the stability of the solvent. Thus, glycerol has excellent solvent power towards group 1A - group VII A alkali metal halides. However, glycerol tends to undergo dehydration to yield volatile fragments which leads to an increase in pressure and therefore to electric breakdown. The difficulty was partially mitigated by using hexane 1,2,3-triol and hexane 2,4,5-triol.

In addition to Octoil and glycerol, some solvents of the poly-hydroxy family have been considered:

Carbowax 600(polyethylene glycol of average molecular weight 570 - 630). This solvent possesses a low vapor pressure (5.3×10^{-6} mm Hg at 100° C). Also the presence of free hydroxyl groups causes relatively large amounts of ionic materials to be dissolved due to the formation of hydrogen bonded solvates. Thus, phenol, zinc sulfocarbolate and boric acid are soluble in Carbowax 600. Various Carbowax solvents appear to be generally promising as solvents.

Esters. The solvents in this category may be considered together:

	Mid boiling point at 5 mm Hg
di isooctyle phthalate	235° C
di tridecyl phthalate	286° C
di isodecyl phthalate	256° C
di hexyl phthalate	210° C
-ethyl hexyl phthalate	
dibutyl phthalate	
tricresyl phosphate	220° C

4.3 Surface Tension

Decreased surface tension should lead to an improvement in the charge-to-mass ratio under standard conditions. Surface tension values for organic liquids fall within the range of 10 - 100 dyne/cm.

In the case of certain polar solutes containing long hydrocarbon chains, a significant decrease in surface tension was obtained by dissolving these compounds in hydrocarbon solvents. Therefore, these solutes have been investigated since theoretical investigations tend to indicate an increase in charge-to-mass ratio of the liquid with an increase in surface tension of the propellant.

4.4 Viscosity

Viscosity depends upon polymolecular association effects in the solvent. At room temperature, viscosities of pure organic solvents lie between 1 and ca 500 millipoise. Viscosity undoubtedly plays an important role in electrostatic colloidal propulsion since flow rate, droplet size and droplet stability all depend upon this physical property. However, viscosity works against conductivity by decreasing ion mobility in solution.

The most acceptable explanation of the conductivity in organic propellants of the type considered here, is that it is due to ion movement under the action of the electric field. It appears therefore that for a given ion concentration, conductivity will vary inversely with viscosity.

4.5 Conductivity

Mathematical relationships for dielectrics and ionization phenomena are too well known to repeat here. Our method has been to decrease the resistivity of organic liquids by adding polar organic and inorganic solute to them.

4.6 Polar Solutes

Solutions of solutes in polar solvents cause a polarization of the surrounding solvent molecules. This polarization is basically electrostatic in nature and one observable effect is an increase in the conductivity of the solutions.

Alkali-metal Sulfonates. Solutions of these materials in polar organic solvents caused substantial decreases in the surface tension of the pure solute. However, only insignificant changes in the conductivity of the solvent were detected. The decrease in surface tension is rationalized in terms of hydrogen bonding and solvation of the cation and hydrocarbon chain. These materials do not appear to offer any advantages which would warrant further investigation.

Tetraalkylammonium Salts. The best solutes found appear to be either ionic, such as the tetraalkylammonium salts or those with highly polarizable anions such as alkyl bromides and chlorides. Polyphosphoric acid was also shown to be a useful additive for decreasing solvent resistivity; however, the unpredictable behavior during charging for solutions containing polyphosphoric acid mitigates against their usefulness. Attempts to form phosphate salts of urea and quanidine were only partially successful.

Miscellaneous Solutes. Results of tests using such solutes as antimony trichloride, silver nitrate, tellurium tetrabromide, uranyl nitrate, lithium iodide, aluminum bromide, aluminum chloride, sodium chloride, and sodium azide are summarized in Table I.

Surface Active Agents. A number of surface active agents have been evaluated. These materials fall into the non-ionic, cationic, and anionic categories.

Among the non-ionic types, octylphenoxyethanols were used. These materials are differentiated according to whether alkyl or aryl groups are bound to oxygen. Such compounds have been used industrially as oil soluble detergents.

The cationic surface active agents which were tested are: stearyldimethylbenzyl-ammonium chloride, methyldodecylbenzyltrimethyl-ammonium chloride, and octylphenoxyethoxyethyldimethylbenzylammonium.

These cationic agents are related structurally to triton in that they are alkyl derivatives of quaternary benzylammonium chloride. The anionic surface active agents which were studied in the present program are sodium salts of alkyaryl polyether sulfonates. Also, carboxylic acid sodium salts such as those of polymeric napthlyene derivatives were examined. A second type of cationic surface tension agent which has been used is the class of polyoxylated quaternary amines.

These surface active agents were chosen because it was anticipated that they would: (a) be soluble in organic solvents, (b) lower the surface tension of the solvent, (c) decrease the resistivity of the solvent, and (d) not react chemically with the solvent. These expectations were partially realized. However, difficulties have been experienced in achieving sufficiently concentrated solutions. The observed variations in the above properties which have thus far been obtained with cationic and anionic surface active agents appear sufficiently encouraging to warrant a more extensive study; in particular, more generally useful solvents can possibly be found. Along these lines, experiments have been initiated using polyhydroxylated agents which are structurally related to glycerol. Further tri- and tetra-hydroxylated cyclohexane derivatives as well as tetra- and penta-hexane and heptane derivatives have been determined to be of interest.

Tests with various concentrations of sodium dinonyl naphthalene solfonate (NADNNS) in Octoil resulted in variations of the surface tension from 30 to 20 dynes/cm.

TABLE I PHYSICAL PROPERTIES OF PROPELLANTS

Solvent	Solute	Resistivity ohms-cm	Density gm/cm^3	Surface Tension dynes/cm	Remarks
Carbowax 550	10% Polyphosphoric Acid & Urea	3.5×10^5	1.103	37.5	Oversaturated
Carbowax 550	Potassium Perchlorate	1.5×10^5	1.167	36	Fair
Octoil	Potassium Perchlorate	$> 10^9$			Fair
Carbowax 550	Disodium Ethylenediamine-Tetraacetate	1.9×10^6	1.09	37.6	Fair
Octoil	Disodium Ethylenediamine-Tetraacetate	$>10^8$			
Carbowax 550	Tetrabutylammonium Iodide	4.3×10^5			Fair
Octoil	Tetrabutylammonium Iodide	$> 10^8$			Poor
Octoil	Sodium Bisulfate	$> 10^9$			Insoluble
Carbowax 550	Cadmium Bromide	3.5×10^5			Fair
Octoil	Cadmium Bromide	$> 10^9$			Poor
Carbowax 550	Sodium Bisulfate	1.4×10^5	1.1	36	Fair
Carbowax 550	1-Naphthol-4-Sulfonic Acid	2.4×10^5	1.13	29	Good
Octoil	1-Naphthol-4-Sulfonic Acid				Fair

TABLE I (Continued)

Solvent	Solute	Resistivity ohms-cm	Density gm/cm^3	Surface Tension dynes/cm	Remarks
Carbowax 550	Urea	9×10^5	1.11	29	Fair
Octoil	Urea	$>10^9$			Poor
Tricresyl Phosphate	Urea	$>10^8$			Poor
Carbowax 550	Cupferon	4×10^5	1.10	33	Fair
Octoil	Cupferon	$>10^8$			Fair
Niax	Cupferon	$>10^8$			Fair
Tricresyl Phosphate	Cupferon	$>10^8$			Fair
Pluracol 410 *	Trisodium Phosphate	8×10^5			Crystallizes
Tricresyl Phosphate	Octadecylamine				
Carbowax 550	Sodium Bisulfate and Urea	1.5×10^5	1.107	36.5	
Carbowax 550	8% Lithium Iodide	1.2×10^5			
Carbowax 550	8% Lithium Iodide and Sodium Bisulfate	1.10^5	1.154	37	

* Wyandotte Chemical Company

TABLE I (Continued)

Solvent	Solute	Resistivity ohms-cm	Density gm/cm^3	Surface Tension dynes/cm	Remarks
Carbowax 550	Aluminum Iodide	4.7×10^4			
Tricresyl Phosphate	Aluminum Iodide	1.5×10^5			
Pluracol 410 *	Aluminum Iodide	1.1×10^5			
Octoil	Aluminum Iodide	5×10^6			
Glycerin	Sodium Chloride	6×10^3			
Carbowax 550	Sodium Chloride	4.2×10^5			
Tricresyl Phosphate	Lithium Iodide	1.7×10^5			
PG 1200	Lithium Iodide	1.3×10^5			
Octoil	Tetra-N-Butylammonium Picrate	4.2×10^5			
Carbowax 550	5% Polyphosphoric Acid	2.4×10^5			
Carbowax 550	10% Polyphosphoric Acid	1.7×10^5			
Carbowax 550	20% Polyphosphoric Acid	1.1×10^5			
Carbowax 550	4% Lithium Iodide	9×10^3			

* Wyandotte Chemical Company

TABLE I (Continued)

Solvent	Solute	Resistivity ohms-cm	Density gm/cm^3	Surface Tension dynes/cm	Remarks
Carbowax 550	8% Lithium Iodide	7×10^3			
Carbowax 550	4% Tetra-N-Butylammonium Picrate	1.4×10^5			
Carbowax 550	6% Tetra-N-Butylammonium Picrate	7×10^4			
Carbowax 550	10% Tetra-N-Butylammonium Picrate	5×10^4			
Pluracol 410 *	5% Lithium Iodide	2.5×10^4			
Carbowax 550	20% Lithium Bromide	2.4×10^4			
Squalene	Sodium Bisulfate				Insoluble
Squalene	Tetra-N-Butylammonium Picrate				Low Solubility
1,2,6 Hexanetriol **	Tetra-N-Butylammonium Picrate	9×10^5			
1,2,6 Hexanetriol **	Potassium Perchlorate	7×10^5			
1,2,6 Hexanetriol	Potassium Hydroxide	2×10^5			

* Wyandotte Chemical Company
** Columbia Organic Chemicals Co., Inc.

TABLE I (Continued)

Solvent	Solute	Resistivity ohms-cm	Density gm/cm^3	Surface Tension dynes/cm	Remarks
Carbowax 550	40% Triton X-45	5.3×10^6			
Carbowax 550	25% Hyamine 35000***	1×10^5			
Octoil	25% Hyamine 35000***				Insoluble
Carbowax 550	N-cetyl N-ethyl Morpholinium Ethosulfate (G-263)****	1.6×10^5			
Carbowax 550	G-3570****				Insoluble
Octoil	G-3570****				Insoluble
Arquad C-50*****		8×10^4			
Arquad S-50*****		7×10^4			Removal of Volatile Components leaves a Light Jelly
Ethoquad C/12*****		1.4×10^5			
Ethoquad C/25*****		2×10^5	1.074	34.2	

*** Rohm & Haas
**** Atlas Chemical Industries, Inc.
***** Armour Industrial Chemical Company

TABLE I (Continued)

Solvent	Solute	Resistivity ohms-cm	Density gm/cm^3	Surface Tension dynes/cm	Remarks
Priminox ***		2×10^8			
1,2,6 Hexanetriol **		7×10^7	1.1	31	
Triton X-45 ***		1×10^8			Refluxed
Triton GR-7 ***		7×10^7			
G-3300 ****		3.6×10^5			
G-3634A ****		2.5×10^5			Refluxed
Atlox-3404 ****		4×10^7			
Atlox-3335 ****		3×10^7			Refluxed
Carbowax 550	Dibenzyl Dimethyl Ammonium Chloride	1.2×10^5			
1,2,6 Hexanetriol	Dibenzyl Dimethyl Ammonium Chloride	2.2×10^5			

** Columbia Organic Chemicals Co., Inc.
*** Rohm & Haas
**** Atlas Chemical Industries, Inc.

TABLE I (Continued)

Solvent	Solute	Resistivity ohms-cm	Density gm/cm^3	Surface Tension dynes/cm	Remarks
Carbowax 550	Propylene Glycol Monostearate				Insoluble
Carbowax 550	Lithium Bibo rate	2.2×10^6			Low Solubility
Carbowax 550	Molybdic Acid	2×10^6			Suspension
Carbowax 550	Sodium Chloride	7.5×10^5			
Carbowax 550	Lanathium Chloride	7×10^5			
Carbowax 550	Picryl Chloride	1.3×10^6			
Octoil	Picryl Chloride	1×10^8			
Carbowax	Armosul 16 ****	1.6×10^5	1.084	34	Very Soluble
Octoil	Armosul 16 *****				Crystallizes
Carbowax 550	Arquad C-50 *****				Insoluble
Octoil	Arquad C-50 *****				Insoluble
Squalene	Arquad C-50 *****				Insoluble
Squalene	Urea				Insoluble

***** Armour Industrial Chemical Company

TABLE I (Continued)

Solvent	Solute	Resistivity ohms-cm	Density gm/cm^3	Surface Tension dynes/cm	Remarks
G-3634 *****	Dibenzyldimethyl ammonium chloride	2.1×10^5			
G-3634 *****	1-Naphthol-4-Sulfonic Acid	2.2×10^5			
Glycerol	Sodium Chloride	1.6×10^5			
Pluracol 410 *	Potassium Hydroxide	1.2×10^6			Saturated solution
Carbowax 550	Tetrapotassium Pyrophosphate				Insoluble
Octoil	Tetrapotassium Pyrophosphate				Insoluble
Carbowax 550	Sodium Borohydride	1.3×10^5			
Hexanetriol **	Tetrapotassium Pyrophosphate				Insoluble
Tricresyl Phosphate	Tetrapotassium Pyrophosphate				Insoluble
Carbowax 550	Hexanetriol + Potassium Hydroxide	1×10^5			
Carbowax 550	Potassium Hydroxide	3.2×10^5			Saturated Solution

* Wyandotte Chemical Company
** Columbia Organic Chemicals Co., Inc.
***** Armour Industrial Chemical Company

TABLE I (Continued)

Solvent	Solute	Resistivity ohms-cm	Density gm/cm^3	Surface Tension dynes/cm	Remarks
Carbowax 550	Boron Fluoride	1.5×10^5			Very good solubility - exothermic reaction
Carbowax 550	Ethyl Ether	2.4×10^5			Fumes in air after refluxing two days
Carbowax 550	1-Propanesulfonyl Chloride	$2.7\text{-}8 \times 10^5$			
Carbowax 550	Tetra-N-Hexyl-Ammonium Iodide	2.5×10^5			Good solubility with heat
Carbowax 550	3-Methyl-1-Butane-Sulfonic Acid Sodium Salt	1.9×10^5			Saturated Solution
Carbowax 550	Tetrathylammonium Perchlorate	2.2×10^5			Saturated Solution
Octoil	4% Tetra-N-Hexyl-Ammonium Iodide	2×10^6			Over saturated
Octoil	G-3570*****	1.5×10^7			
Carbowax 550	G-3570*****				Insoluble
G-3634*****		2.2×10^5	1.0185	24.8	

***** Armour Industrial Chemical Company

TABLE I (Continued)

Solvent	Solute	Resistivity ohms-cm	Density gm/cm^3	Surface Tension dynes/cm	Remarks
Octoil	Octadecylamine				Crystallizes
Octoil	Sodium Metasilicate				Insoluble
Octoil	Calgonite	$> 10^9$		28.1	
Carbowax 550	None	8.2×10^5		37	
Carbowax 550	10% Polyphosphoric Acid and Calgonite	6×10^5		26.5	
Carbowax 550	4% Aluminum Iodide	1.4×10^5		36.8	
Carbowax 550	4% Aluminum Iodide and 4% NADNNS			28.8	
Carbowax 550	Calgonite	3×10^5		36.8	
Carbowax 550	N, N-Diphenylformamide	3.7×10^6		35.7	
Carbowax 550	Octadecylamine				Solid at room Temperature
Carbowax 550	1-Naphthol-4-Sulfonic Acid	2.4×10^5		28.4	
Carbowax 550	SDMI	5×10^5		35	
Octoil	None	$> 10^9$		29	

TABLE I (Continued)

Solvent	Solute	Resistivity ohms-cm	Density gm/cm^3	Surface Tension dynes/cm	Remarks
Octoil	4% Tetra-N-Butylammonium Picrate	4.7×10^5		28.7	
Octoil	1% NaDNNS	$> 10^9$		25	
Octoil	4% Tetra-N-Butylammonium Picrate and 5% Dioctyl Sodium Sulfosuccinate	5.7×10^5		27.4	

5. THEORETICAL ANALYSIS OF SYSTEM PERFORMANCE

During previous programs (References 3 and 4), a theoretical investigation of system performance was carried out in order to provide understanding of the experimentally observed phenomena and to predict performance trends. The results of a series of performance mapping experiments were shown (Reference 4) to be in excellent agreement with the theoretical predictions. In this section, we shall review and interpret these theoretical results and sketch their implications for system performance.

The ultimate goal of the theoretical investigation is to predict the variation of system performance, as reflected in

q/m	=	droplet charge-to-mass ratio
I	=	beam current
F	=	beam thrust
v	=	droplet exhaust velocity
P	=	beam power

with the controllable operating parameters, i.e.,

$\dot{m}$	=	mass flow rate
V	=	voltage
ω	=	nozzle rotating speed
T	=	temperature

propellant, typified by such properties as

γ	=	surface tension
ϵ	=	capacitivity
ν	=	kinematic viscosity
ρ_m	=	mass density
σ	=	conductivity

and nozzle and electrode geometries, typified by

L	=	characteristic scale length (e.g., distance from nozzle to extractor electrode)

shape parameters such as r/L where r = nozzle radius.

In seeking this goal, we have followed a purely phenomenological approach. We assume that droplets are charged by induction and are formed by either i) extraction, wherein droplets have a characteristic size

of roughly the film thickness at the edge of the nozzle, of ii) disintegration, wherein, because the film is relatively thick, droplets have a characteristic size dictated by a Rayleigh-like stability criterion. We further assume that, in both of these modes, all droplets have a single, uniform charge-to-mass ratio, for any fixed operating condition. By this simplified approach, we thus circumvent (but don't eliminate) the details of the instabilities which are the actual mechanism for forming and charging the droplets; inasmuch as these instabilities are ill understood, even in the absence of electric forces, no other approach is feasible. By postulating a unique droplet charge-to-mass ratio, we automatically exclude not only all droplets of any other charge-to-mass ratio but also all ions, either of propellant or ambient gas. Indeed, we ignore all plasma effects due to energetic processes in the ambient gas.

In this approach, the entire system performance is completely specified by the charge-to-mass ratio via

$$\begin{aligned} I &= \dot{m}\,(q/m) \\ F &= \dot{m}\,(2V)^{1/2}\,(q/m)^{1/2} \\ v &= (2V)^{1/2}\,(q/m)^{1/2} \\ P &= \dot{m}\,V\,(q/m) \end{aligned} \tag{1}$$

The charge-to-mass ratio, however, is given (Reference 4) is an explicit function of controllable elements by

$$q/m = \begin{cases} \hat{(q/m)}_1 g_1(\lambda) & \lambda > f_1(\Gamma),\ \text{E mode} \\ \hat{(q/m)}_3 \left[g_3 (\lambda^{1/3}/\Gamma^{2/3})\right]^3 & \lambda \ll f_1(\Gamma),\ \text{D mode} \end{cases} \tag{2}$$

where the parameters $\hat{(q/m)}_1$, $\hat{(q/m)}_3$, λ and Γ are given explicitly as

$$\hat{(q/m)}_1 = C_1 D^{1/3} \frac{\epsilon V}{L^{1/3}}\, \dot{m}^{-1/3} \omega^{2/3} (r/L)^{2/3} (\rho_m{}^2 \nu)^{-1/3} [1 - \exp(-\sigma\tau/\epsilon)] \tag{3}$$

$$\hat{(q/m)}_3 = C_3{}^3 \frac{\epsilon^2 V^3}{L^3} (\rho_m \gamma)^{-1} [1 - \exp(-\sigma\tau/\epsilon)]^2 \tag{4}$$

$$\lambda = \frac{C_1 D}{2\pi B K_4{}^2)^2} \frac{L^3}{\epsilon V^2}\, \dot{m}\, \omega^2\, \nu^{-1} [1 - \exp(-\sigma\tau/\epsilon)] \tag{5}$$

$$\Gamma = \left(\frac{C_1 D^{1/3}}{C_3^3}\right)^{1/2} \frac{L^{4/3}}{\epsilon^{1/2} V} \dot{m}^{-1/6} \omega^{1/3} (r/L)^{1/3} \left(\frac{\gamma^3 \rho_m}{\nu}\right)^{1/6} \qquad (6)$$

$$[1 - \exp(-\sigma\tau/\epsilon)]^{-1/2}$$

B, C_1, C_3, D, K_4 are dimensionless parameters dependent primarily on geometry

$\bar{\tau}$ = characteristic time available for charging a droplet

The functions f_1 and f_3 are monotonically decreasing functions mapping the interval (0, 1) onto the interval (0, ∞). We denote by g_1 and g_3 the functions inverse to f_1 and f_3, respectively, i.e., the functions for which $f_k(g_k(x)) = x$ for all x, k = 1, 3. (These functions are inverse functions in the same sense that the logarithmic and exponential functions are inverse functions.) Consequently, g_1 and g_3 are monotonically decreasing functions which map the interval (0, ∞) onto the interval (0, 1). Here and below, the subscripts "1" and "3" refer to the extraction (E) and disintegration (D) modes, respectively. Although the functions f_1, f_3, g_1, g_3 cannot be specified explicitly without a complete solution of the space-charge problem, their asymptotic behavior can be determined and establishes the system performance in both the weak and strong space-charge limits; the predicted performance in these limits is summarized later in this section. For the present, however, it is more instructive to examine the structure of the results presented above.

We note first that the system performance is dictated by the two dimensionless parameters λ and Γ. Via (5) and (6), each experiment (i.e., each set of controllable elements) corresponds to a unique point in λ-Γ space. Moreover, these values of λ and Γ determine whether droplets are formed by disintegration or extraction. As shown in the accompanying sketch, the system operates in the D or E mode accordingly as the operating point lies above or below the curve $\lambda = f_1(\Gamma)$. The strength of space-charge effects is measured by the dimensionless parameter e_o defined by:

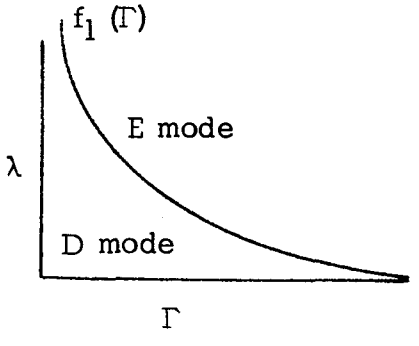

e_o = electric field at edge of nozzle, with propellant flow / electric field at edge of nozzle, without propellant flow

Thus weak and strong space-charge effects correspond to $e_o \simeq 1$ and $e_o \ll 1$, respectively. It is readily demonstrated that the contours e_o = constant = η, say, take the form

$$\lambda = \begin{cases} [f_1(\eta)]\,(\Gamma/\eta)^2 & 0 \le \Gamma \le \eta \\ f_1(\eta) & \eta \le \Gamma \le \infty \end{cases} \qquad (7)$$

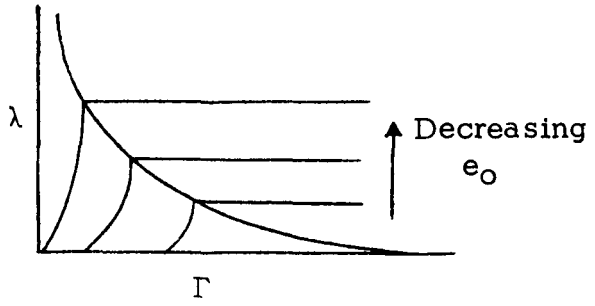

Thus, as shown in the accompanying sketch, the contours of constant space-charge effects are represented, in $\lambda - \Gamma$ space, by parabolas in the D region and horizontal lines in the E region. Moreover, it is clear that strong and weak space-charge effects correspond to operating points located in the regions shown in the accompanying sketch. It is instructive to consider separately the influence of each controllable element upon system performance.

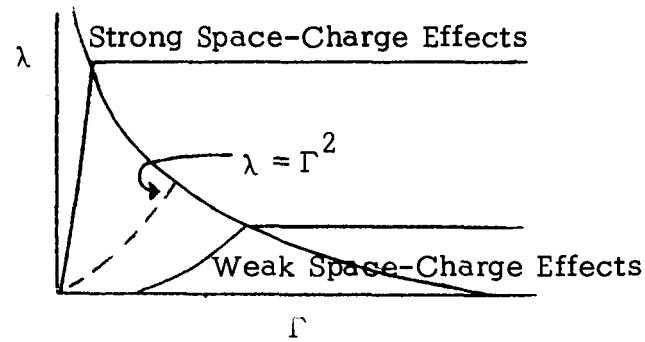

The accompanying sketch shows the direction of the path followed by the operating point as the corresponding controllable element is <u>increased</u>. As we noted above, space-charge effects became stronger as e_o decreases, i.e., as λ (or $\mu \equiv \lambda^{1/3}/\Gamma^{2/3}$) increases and the system is in the E (or D) mode. Therefore, as a controllable parameter increases, space-charge effects become stronger if, and

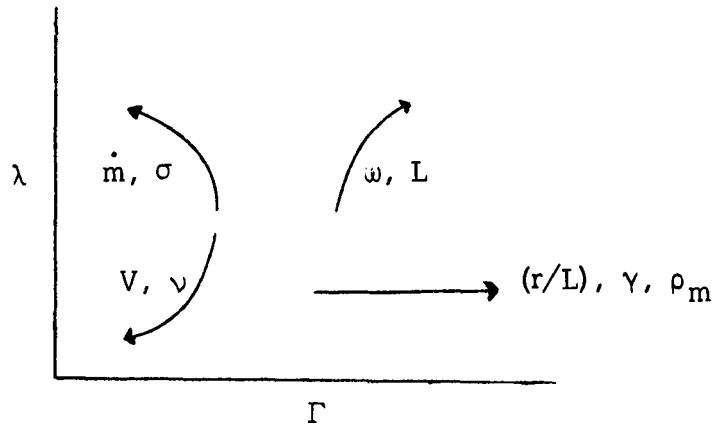

only if, λ (or $\mu \equiv \lambda^{1/3}/\Gamma^{2/3}$) is an increasing function of that parameter and the system is in the E (or D) mode. The accompanying table shows the direction of changes in space-charge effects with increases in various operating parameters.

Parameter	E-mode Charge	D-mode Charge
$\dot{m}$	Increase	Increase
ω	Increase	Increase
V	Decrease	None
ρ_m	None	Decrease
γ	None	Decrease
ν	Decrease	Decrease
σ	Increase	Increase

Effect of Parameter Increases Upon Space-Charge Effects

By considering the path of the operating point in $\lambda - \Gamma$ space, it is possible to determine the variation of any performance characteristic with changes in controllable elements. We now illustrate this by considering the droplet charge-to-mass ratio; completely analogous results may be obtained for the beam current, thrust, power or droplet exhaust velocity. We consider first the influence of voltage upon charge-to-mass ratio. Since $\Gamma \sim V^{-1}$ and f_1 is a decreasing function, $f_1(\Gamma)$ vanishes for sufficiently small V and then increases steadily. Conversely, $\lambda \sim V^{-2}$, and λ decreases steadily for increasing V. Consequently, the system operates in the E mode ($\lambda > f_1(\Gamma)$), for sufficiently small V and in the D mode for larger V. In the E mode, $(q/m)_1 \approx V$ while e_o also increases with increasing V, since $\lambda \sim V^{-2}$. Thus $q/m = (q/m)_3 \approx V^3$ and e_o is independent of V since μ is independent of V. Thus $q/m = (q/m)_3\, e_o^3$ is an increasing ($\sim V^3$) function of V in the D mode also. In summary, the charge-to-mass ratio is an increasing function F, for all V. The transition, if any, to strong space-charge effects is determined by the values of the other parameters being held constant while V is varied.

Completely analogous considerations show that as $\dot{m}$ alone is varied, the system operates in the E mode for sufficiently small and large $\dot{m}$, and in the D mode for some intermediate range of $\dot{m}$, if at all. Likewise q/m is a steadily decreasing function of $\dot{m}$, for all $\dot{m}$, in both the E and D modes. Similarly, as ω alone is varied, the system operates in the D mode for sufficiently small ω and in the E mode for all larger ω. In the D mode, q/m is a decreasing function of ω. In the E mode, q/m may possibly increase with ω for all sufficiently large ω. Strong space-charge effects necessarily occur for sufficiently large $\dot{m}$ or ω.

The effects of varying a single propellant property are determined similarly. The system operates in the D and E modes for sufficiently small and large ρ_m, respectively. Charge-to-mass ratio is a steadily decreasing function of ρ_m, for all ρ_m. The transition, if any, to strong space-charge effects, is determined by the other parameters. The influence of γ upon q/m is the same as that of ρ_m, except that q/m approaches a finite limit, rather than zero, for sufficiently large γ. The system operates in the E and D modes for sufficiently small and large ν, respectively. In the E mode, q/m is an increasing function of ν for sufficiently small ν but may be decreasing for some range of larger ν. In the D mode, q/m is a steadily increasing function of ν. Strong space-charge effects necessarily occur for sufficiently small ν. Finally, the system operates in the E mode for at least sufficiently small σ and in the D mode, if at all, only for all larger values of σ. In both the E and D modes, q/m is a steadily increasing function of σ, and approaches a finite limit for sufficiently large σ. The transition, if any, to strong space-charge effects is determined by the other parameters held constant while σ is varied. The influence of conductivity upon charge-to-mass ratio is characteristic. Indeed, for sufficiently high propellant conductivity, all the system performance characteristics (charge-to-mass ratio, current, thrust, power, exhaust velocity) approach asymptotically a limit which is independent of conductivity.

The detailed, explicit variation of system performance in the strong and weak space-charge limits is obtained straightforwardly and is now summarized from Reference 4. In the strong space-charge limit, for both the D and E modes, we obtain

$$q/m = (q/m)^* = (2\pi B K_4^2)^2 D^{-2/3} \frac{\epsilon^2 V^3}{L^{10/3}} \dot{m}^{-4/3} \omega^{-4/3} (r/L)^{2/3} \left(\frac{\nu}{\rho_m}\right)^{2/3} \quad (8)$$

$$I = I^* \equiv \dot{m}\,(q/m)^* = (2\pi B K_4^2)^2 D^{-2/3} \frac{\epsilon^2 V^3}{L^{10/3}} \dot{m}^{-1/3} \omega^{-4/3} (r/L)^{2/3} \left(\frac{\nu}{\rho_m}\right)^{2/3} \quad (9)$$

$$F = F^* \equiv \dot{m}\,(2V)^{1/2}\,(q/m)^{*1/2}$$
$$= (2\pi B K_4^2)\,2^{1/2} D^{-1/3} \frac{\epsilon^{1/2} V^2}{L^{5/3}}\,\dot{m}^{1/3}\,\omega^{-2/3}\,(r/L)^{1/3}\left(\frac{\nu}{\rho_m}\right)^{1/3} \quad (10)$$

$$v = v^* \equiv (2V)^{1/2}\,(q/m)^{*1/2}$$
$$= (2\pi B K_4^2)\,2^{1/2} D^{-1/3} \frac{\epsilon^{1/2} V^2}{L^{5/3}}\,\dot{m}^{-2/3}\,\omega^{-2/3}\,(r/L)^{1/3}\left(\frac{\nu}{\rho_m}\right)^{1/3} \quad (11)$$

$$P = P^* \equiv \dot{m}\,V\,(q/m)^*$$
$$= (2\pi B K_4^2)^2 D^{-2/3} \frac{\epsilon V^4}{L^{10/3}}\,\dot{m}^{-1/3}\,\omega^{-4/3}\,(r/L)^{2/3}\left(\frac{\nu}{\rho_m}\right)^{2/3} \quad (12)$$

In the weak space-charge limit, the performance is different in the two modes. In the extraction mode, we obtain

$$q/m = \hat{(q/m)}_1$$
$$= C_1 D^{1/3} \frac{\epsilon_o V}{L^{1/3}}\,\dot{m}^{-1/3}\,\omega^{2/3}(r/L)^{2/3}(\rho_m^2\nu)^{-1/3}[1-\exp(-\sigma\tau/\epsilon)] \quad (13)$$

$$I = \hat{I}_1 \equiv \dot{m}\,\hat{(q/m)}_1$$
$$= C_1 D^{1/3} \frac{\epsilon_o V}{L^{1/3}}\,\dot{m}^{2/3}\,\omega^{2/3}\,(r/L)^{2/3}(\rho_m^2\nu)^{-1/3}[1-\exp(-\sigma\tau/\epsilon)] \quad (14)$$

$$F = \hat{F}_1 \equiv \dot{m}\,(2V)^{1/2}\,\hat{(q/m)}_1^{1/2} \quad (15)$$
$$= (2C_1)^{1/2} D^{1/6} \frac{\epsilon_o^{1/2} V}{L^{1/6}}\,\dot{m}^{5/6}\omega^{1/3}\,(r/L)^{1/3}(\rho_m^2\nu)^{-1/6}[1-\exp(-\sigma\tau/\epsilon)]^{1/2}$$

$$v = \hat{v}_1 \equiv (2V)^{1/2}\,\hat{(q/m)}_1^{1/2}$$
$$= (2C_1)^{1/2} D^{1/6} \frac{\epsilon_o^{1/2} V}{L^{1/6}}\,\dot{m}^{-1/6}\,\omega^{1/3}(r/L)^{1/3}(\rho_m^2\nu)^{-1/6}[1-\exp(-\sigma\tau/\epsilon)] \quad (16)$$

$$P = \hat{P}_1 \equiv \dot{m}\,V\,\hat{(q/m)}_1$$
$$= C_1 D^{1/3} \frac{\epsilon_o V^2}{L^{1/3}}\,\dot{m}^{2/3}\,\omega^{2/3}\,(r/L)^{2/3}\,(\rho_m^2\nu)^{-1/3}[1-\exp(-\sigma\tau/\epsilon)] \quad (17)$$

In the weak space-charge limit of the disintegration mode, we obtain

$$q/m = \hat{(q/m)}_3 = C_3{}^3 \frac{\epsilon_o{}^2 V^3}{L^3} (\rho_m \gamma)^{-1} [1- \exp (-\sigma\tau/\epsilon)]^2 \qquad (18)$$

$$I = \hat{I}_3 \equiv \dot{m} \hat{(q/m)}_3 = C_3{}^3 \frac{\epsilon_o{}^2 V^3}{L^3} \dot{m} (\rho_m \gamma)^{-1} [1- \exp (-\sigma \tau/\epsilon)]^2 \qquad (19)$$

$$\begin{aligned} F &= \hat{F}_3 \equiv \dot{m} (2 v)^{1/2} \hat{(q/m)}_3{}^{1/2} \\ &= 2^{1/2} C_3{}^{3/2} \frac{\epsilon_o V^2}{L^{3/2}} \dot{m} (\rho_m \gamma)^{-1/2} [1- \exp (-\sigma\tau/\epsilon)] \end{aligned} \qquad (20)$$

$$\begin{aligned} v &= \hat{v}_3 \equiv (2 V)^{1/2} \hat{(q/m)}_3{}^{1/2} \\ &= 2^{1/2} C_3{}^{3/2} \frac{\epsilon_o V^2}{L^{3/2}} (\rho_m \gamma)^{-1/2} [1- \exp (-\sigma \tau/\epsilon)]^{1/2} \end{aligned} \qquad (21)$$

$$P = \hat{P}_3 \equiv \dot{m} V \hat{(q/m)}_3 = C_3{}^3 \frac{\epsilon_o{}^2 V^4}{L^3} \dot{m} (\rho_m \gamma)^{-1} [1- \exp (-\sigma\tau/\epsilon)]^2 \qquad (22)$$

6. TEST RESULTS

6.1 General

As mentioned earlier, three different vacuum pumping arrangements have been used. The results obtained with the first and third will be described here. Comments on the operation with the second have been given earlier. Tests with the first pumping arrangement primarily involved variations in system geometry. The performance mapping experiments and some massenfilter tests were accomplished with the third pumping arrangement. The procedure for running a test was as follows: First the metering tube containing the propellant (Figure 3) was loaded and the piston's synchronous motor drive started. A period of 2 to 20 minutes was normally required to obtain a steady flow of propellant at the edge of the nozzle. The duration of a test was between 12 minutes and several hours, depending on the chosen mass flow rate. The performance of a test essentially consisted of accomplishing all the measurements shown schematically in Figure 9. The massenfilter readings were, however, taken only on certain tests. Throughout the test, visual observations were made of glows and discharges which might occur within the vacuum chamber. At the conclusion of a test, all of the propellant had precipitated on the collector and in most cases, had been the subject of a transformation. Specifically, in the case of Octoil, the liquid on the collector was dark brown and possessed a much higher viscosity than the original propellant. After each test, the data was reduced and the efficiency calculated using the nomogram shown in Figure 13.

6.2 Tests With First Pumping Arrangement

Tests have been accomplished with a large number of propellants and certain of those have proven to be nearly as good as Octoil plus tetra-n-butyl ammonium picrate, which has traditionally been used. The performance of Carbowax plus lithium iodide or lithium bromide appears particularly promising. These results are shown in Figure 14. Glycerol with lithium iodide, lithium bromide or sodium chloride as additives is capable of very high beam currents. It was, however, nearly impossible to operate above 20 kilovolts without a discharge occurring. The liquid nitrogen cooled collector made it possible to exceed 20 kilovolts, but the data obtained showed poor efficiency as indicated below:

Target Mass Flow mg/sec	Thrust mg	Current microA	Voltage KV	Charge/Mass Coul/Kgm	Efficiency
.028	2.5	1.8	24	64	.23
.035	3	2.5	24	70	.19
.03	3	7.5	23	225	.08
.025	2	4	25	120	.07

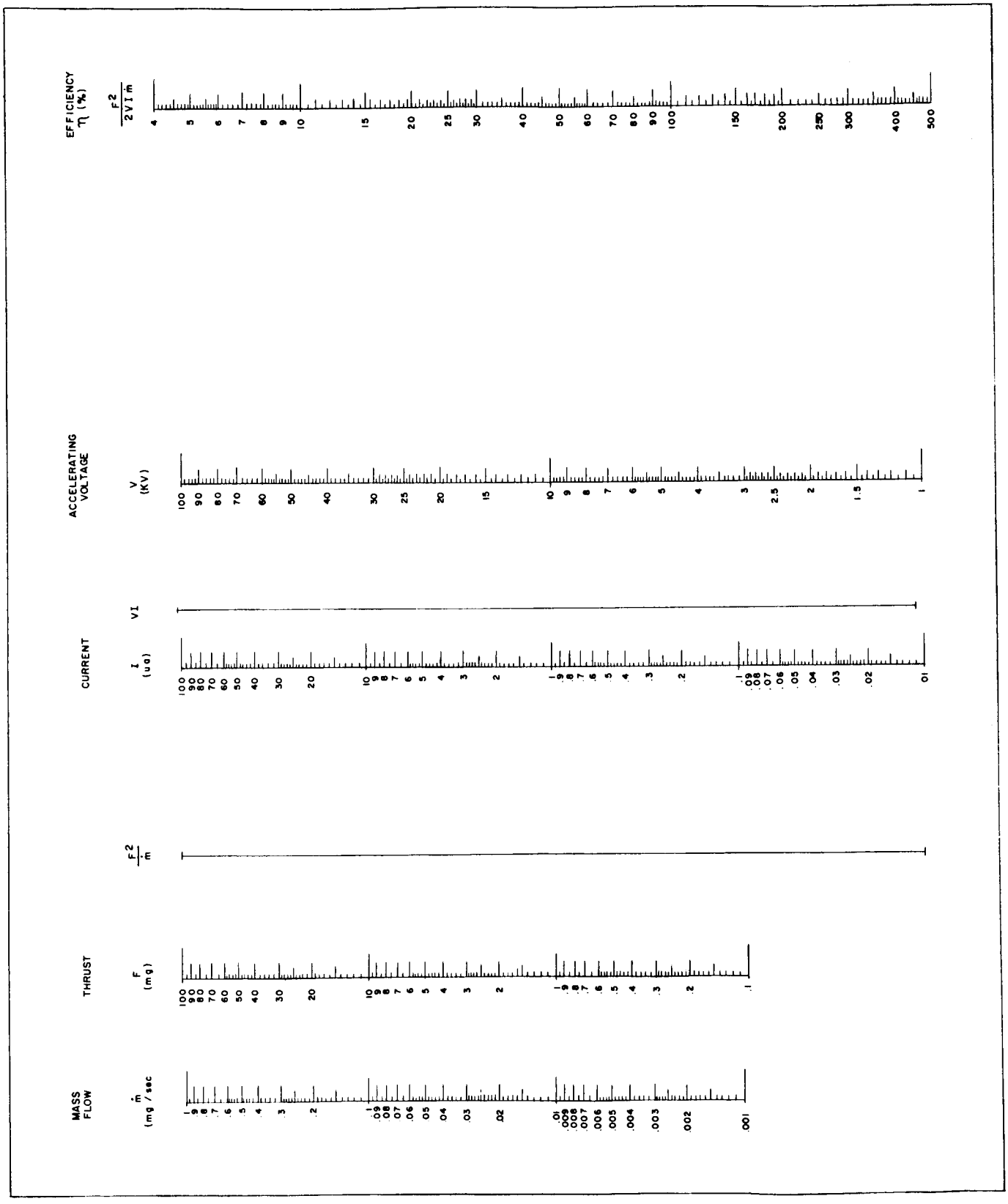

Figure 13. Nomogram for Efficiency Calculations

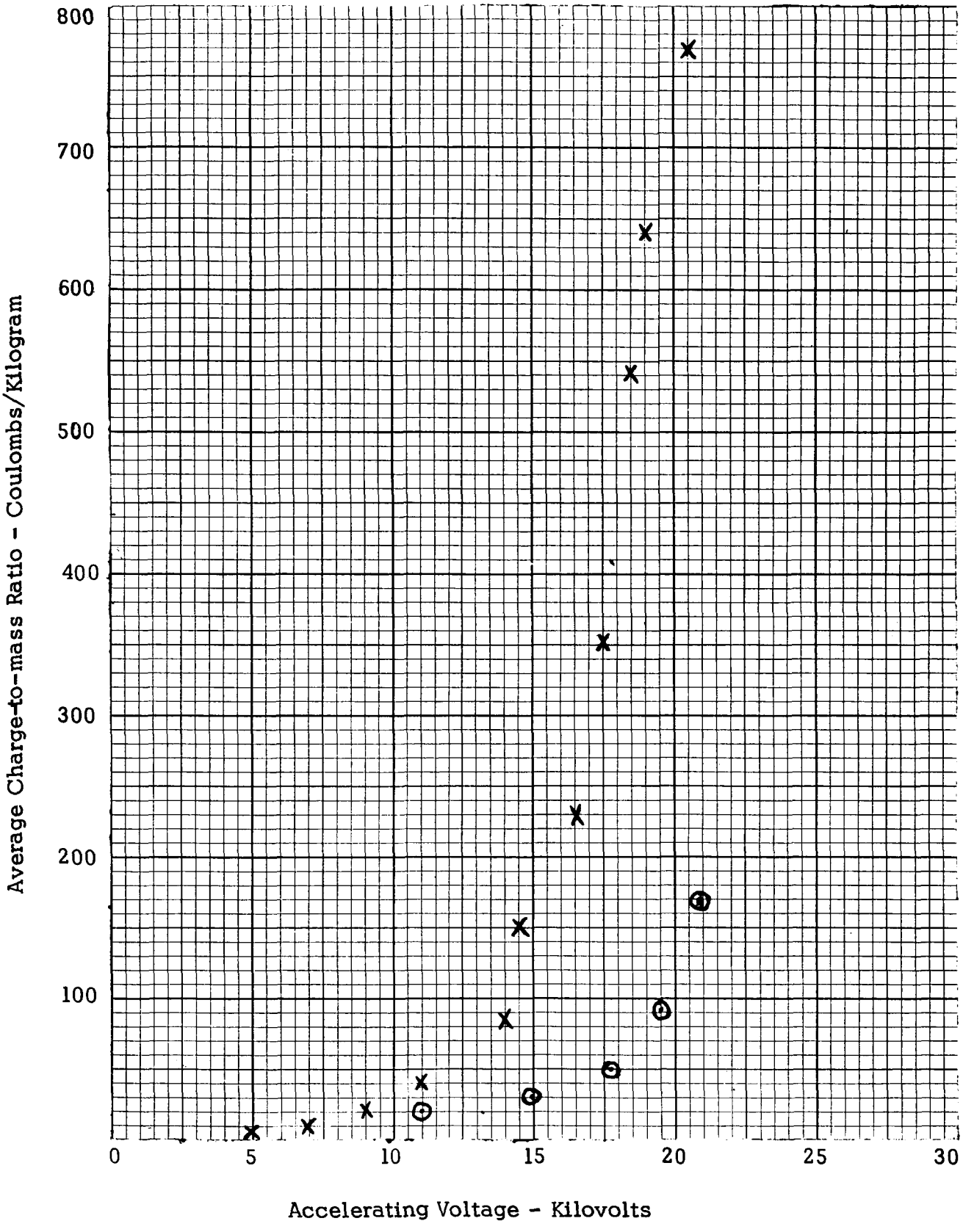

Figure 14. Average Charge-to-mass Ratio Versus Accelerating Voltage for Glycerol + NaCl (X) and Carbowax 550 + LiI (⊙).

On the other hand, tests with Octoil and a number of additives, have shown charge-to-mass ratios of 150 coulombs/kilogram with efficiencies averaging 75%.

Figure 15 shows data recorded on two consecutive days without the vacuum chamber being cleaned between tests. It indicates that the results obtained are fairly reproducible.

Figure 16 shows the variation of beam current with resistivity for the same propellant. This test was accomplished by varying the concentration of TNBAP in Octoil for the three different values of the voltage. The same trend is shown regardless of the voltage. This data correlates well with the theory which has been presented in Section 5.

Considerable improvements to the system were accomplished throughout these tests: the nozzle and its drive were made to operate satisfactorily at speeds up to 15,000 rpm on a continuous basis. The nozzle and the propellant feed system can now safely operate at voltages up to 100,000 volts. In the earlier tests, the collector and the extractor were both moveable by means of a central shaft. During a number of tests in which the position of the extractor alone was changed, it was determined that the optimum position was such that the nozzle protruded from the extractor by about 1/8 of an inch. The position of the collector which gave the highest beam current was about 1/4 of an inch forward of the nozzle. However, in this position, discharges occurred between the nozzle and the collector which caused strong pulses of current to enter the thrust measuring system. It was therefore impossible to accomplish thrust measurements with this configuration.

Improvements in system reliability was obtained by mounting the extractor in a fixed position directly on the glass cylinder of the vacuum chamber. The extractor which performed the best was one mounted with a 1/4-inch clearance in the gap between the extractor and the nozzle. Polishing the extractor resulted in a substantial increase in the voltage, with the average field which can be maintained between the nozzle and the extractor being of the order of 20 kilovolts/millimeter.

Another extractor which was investigated was made of stainless steel and was of essentially toroidal shape with a spacing between the nozzle and the extractor of 1 inch. With this nozzle, it was possible to maintain a voltage of 100,000 volts without discharges, however, the beam current was low.

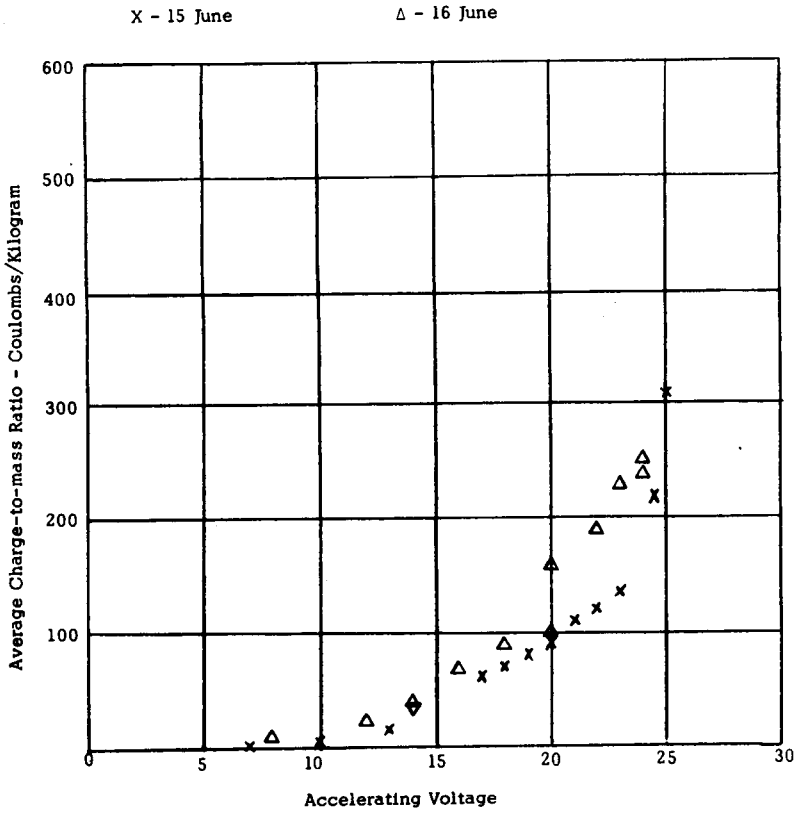

Figure 15. Average Charge-to-mass Ratio Versus Accelerating Voltage (Octoil + TNBAP).

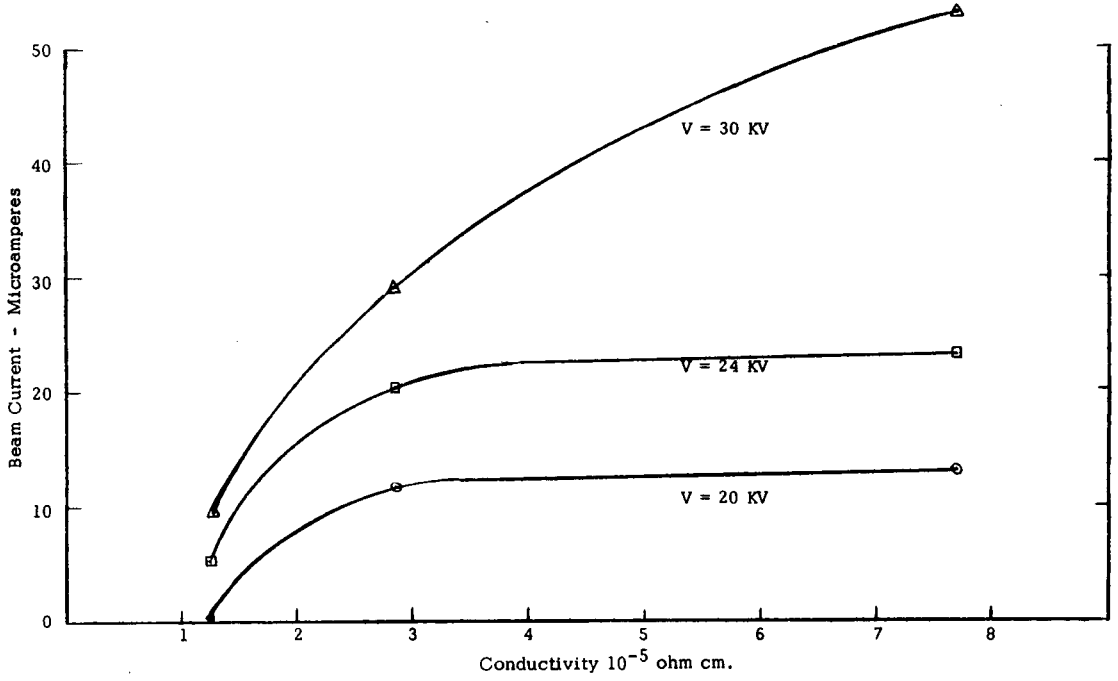

Figure 16. Beam current obtained with the same propellant in which only the conductivity varies for three values of the accelerating voltage. $\dot{m}_T = 1.5 \times 10^{-6}$ kgm/sec, $\omega = 3,500$ rpm. Propellant: Octoil + 1/2%, 1% and 2% TNBAP.

Tests were conducted employing a liquid metal as the propellant. An alloy of gallium and indium was chosen because it satisfied two very desireable conditions. First, it exhibits a very low vapor pressure and, secondly, the eutectic alloy is a liquid at room temperature. This second property greatly simplifies the handling of the propellant.

At the outset, difficulty under test conditions was experienced in wetting the nozzle with the liquid metal. The first attempt to correct this condition was to coat the inside of the stainless steel nozzle with the gallium-indium alloy and then evacuate the chamber. Unfortunately, an oxide layer immediately formed, with the result that the propellant would not wet.

Next, a nozzle heavily coated with gallium (a solid at room temperature) was tried. The chamber was evacuated, the nozzle heated, and an alloy with a greater proportion of indium than the eutectic was introduced as the propellant. It was felt that the melting gallium would carry off the oxide, leaving behind a pure film of gallium that the propellant could wet. The gallium, however, slipped out from beneath the oxide layer leaving the oxide on the surface of the nozzle.

Successful wetting was accomplished by heavily fluxing the nozzle with a solution of hydrochloric acid and zinc chloride while flowing on the eutectic alloy. By careful adjustment of the rotating speed of the nozzle, the high surface tension of the alloy permitted a heavy layer of liquid to be carried on the surface of the nozzle without spilling over the edge. After evacuating the chamber, propellant flow was initiated and the nozzle brought up to operating speed. A uniform film and a steady mass flow of propellant resulted.

Accelerating voltages up to 75 kilovolts were reached before a pre-discharge current began. The maximum beam current obtained corresponded to an average charge-to-mass ratio of less than 1 coulomb/kilogram. The thrust encountered was too small to permit measurement.

The propellant was deposited over the complete surface of the collector in small droplets, indicating a large dispersion of the beam and a very limited breakup of the propellant by the electrostatic field. Attempts to increase the charging proved to be unsuccessful.

The nozzle with a covering of liquid metal is shown in Figure 6.

In order to determine the extent to which secondary emission could account for a part of the collector current, a screen was made and placed immediately in front of the collector. A voltage was applied to this screen and the potential with respect to the collector was varied between +90 and -90 volts. No appreciable change in collector current was noticed. A second experiment in which the voltage between the target and the collector was varied gave similar results.

6.3 Tests With the Third Pumping Arrangement

This pumping arrangement was described earlier in Section 2.8. Essentially, it resulted in a better pumping speed and therefore in a better ultimate vacuum. Thus, it was possible to accomplish tests with Octoil without the pressure increasing above 5×10^{-6} Torr. Massenfilter experiments were accomplished with this system, however, difficulty was encountered in aligning the massenfilter with the beam. As explained earlier in Section 3.3, it is important that the beam enters the massenfilter almost parallel to the axis. The only method to insure this consists of making certain that some beam current reaches the target in the absence of any voltage on the rails. This requires that the quadrupole and the beam be adjusted within 0.005 of a radian. A typical distribution function is shown in Figure 17. It does not correspond to the highest charge-to-mass ratio that had been obtained with the system, however, it does correspond to conditions that were sufficiently stable so that consistent mass filter data could be obtained throughout the test. The data has been integrated and gives the following results:

$$F_m = F(2\,V)^{1/2} \int J_m (q/m)^{-3/2}\, d(q/m) = 6.9 \times 10^{-7} \text{ Newt.}$$

$$I_m = R \int J_m (q/m)^{-1}\, d(q/m) = 1.33 \times 10^{-8} \text{ Ampr.}$$

$$\dot{M}_m = R \int J_m (q/m)^{-2}\, d(q/m) = 4.5 \times 10^{-10} \text{ Kg/sec.}$$

resulting in an efficiency:

$$\eta_m = .88$$

This data has been compared with measurements of thrust, current and mass flow which were as follows:

$$F_t = 6.5 \times 10^{-5} \text{ Newtons}$$

$$I_t = 1.6 \times 10^{-6} \text{ Amp.}$$

$$\dot{m}_t = 4.3 \times 10^{-8} \text{ Kg/sec.}$$

Resulting in a measured efficiency of $\eta_t = .67$.

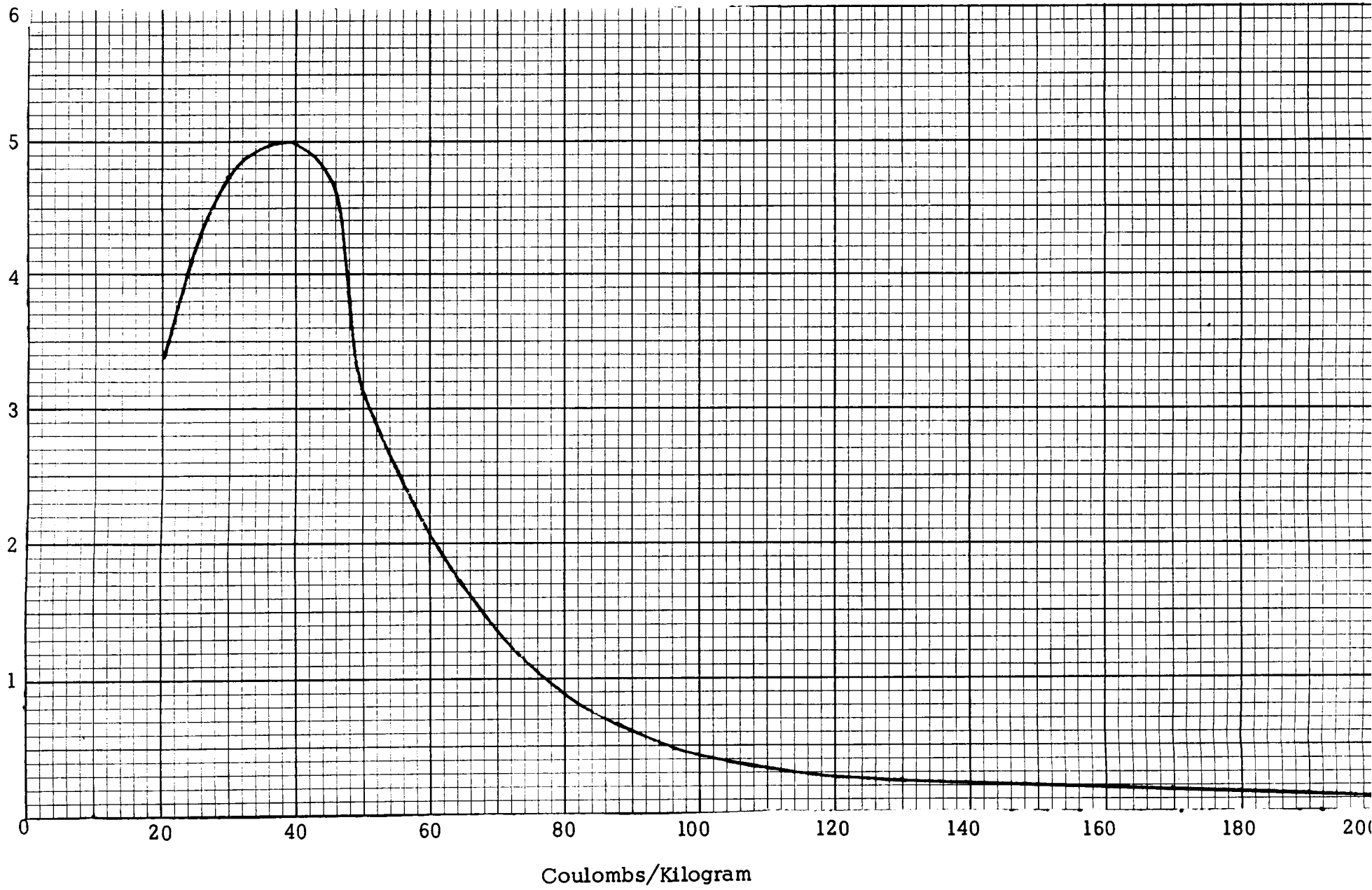

Figure 17. Current Distribution Density as a Function of Charge-to-mass Ratio, Calculated From Quadrupole Measurements.

The fact that the efficiency calculated from the massenfilter measurements is higher than that from thrust measurement may be the result of two factors. The first is the imperfection of the massenfilter as pointed out in Section 3.3 above. The second is the possibility of the presence in the beam of ions of a residual gas which did not show up in the mass filter.

A performance mapping experiment was then undertaken. In a previous program (Reference 4), a performance mapping experiment had been undertaken with a system analogous to what is herein described as the first pumping arrangement. The results obtained here were different and sometimes surprising. Nevertheless, it was decided to continue with this new pumping arrangement rather than revert to the old one as the results would have duplicated those obtained in a previous program.

Three different values of the rotating speed of the nozzle were selected: 1,000, 4,000, and 10,000 rpm. Also selected were three different values of mass flow: .25, 1, and 7.5×10^{-6} kilograms/second. The voltage was varied in steps of 10 kilovolts, between 10 and 100 kilovolts. In most cases, discharges were encountered above 80 kilovolts. All the tests were performed in complete darkness and presented essentially the same observable behavior. Essentially two different modes of operation have been observed:

1) During the initial phase of each test, no glow is visible anywhere. During that period, the total collector current does not exceed 1 microampere and no charging of the propellant is observed.

2) After a time period varying between 5 and 20 minutes, during which the voltage is switched on and off, a glow suddenly occurs as shown in Figure 18. At this point, beam current becomes measureable. It was while this mode remained in effect that the data of Figures 19 to 27 was taken.

Analysis of the Figures 19 to 27 leads to the following observations:

1) The charge-to-mass ratio appears to increase and then decrease with the voltage. This strange behavior was exhibited by all the currents being monitored during the tests, such as, collector current, extractor current and target current. While the tests were being accomplished, no increase in pressure with voltage was noticed, rather the pressure seemed to behave in a manner analogous to that of the current.

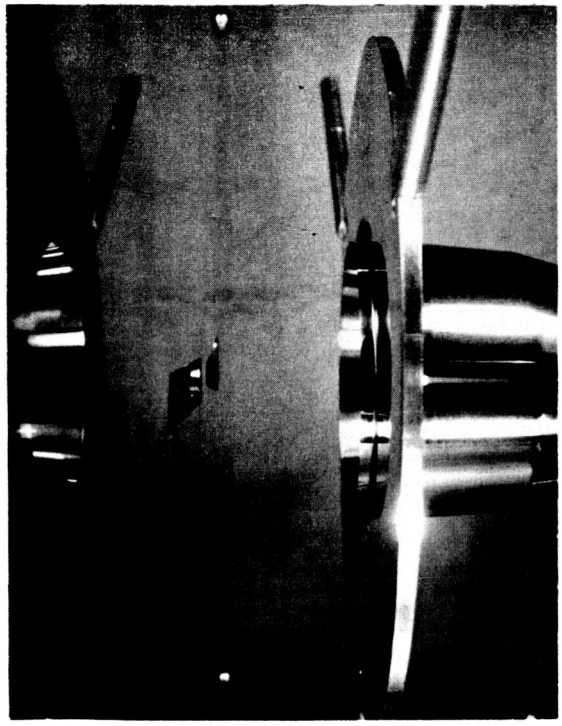

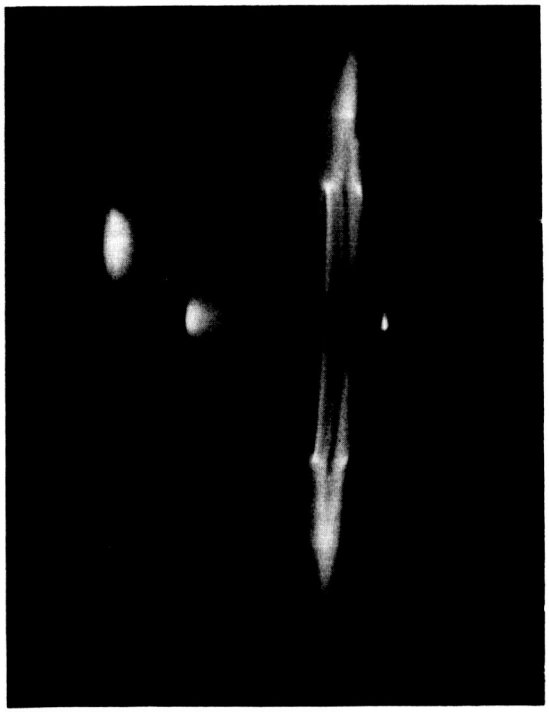

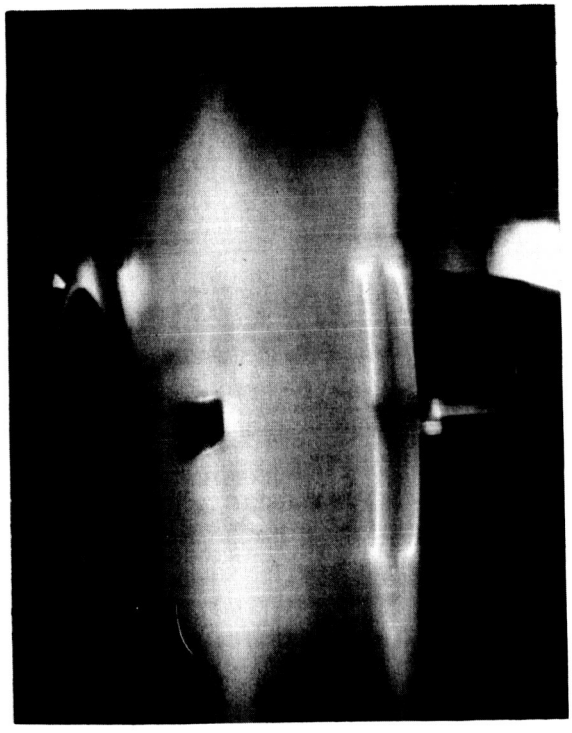

Figure 18. View of the Nozzle, Collector and Beam. Top, at rest.
Bottom Left, with a 10^{-6} Kg/sec beam, at 48 KV with an exposure time of 8 seconds.
Bottom Right, same as above, with exposure time of 60 seconds.

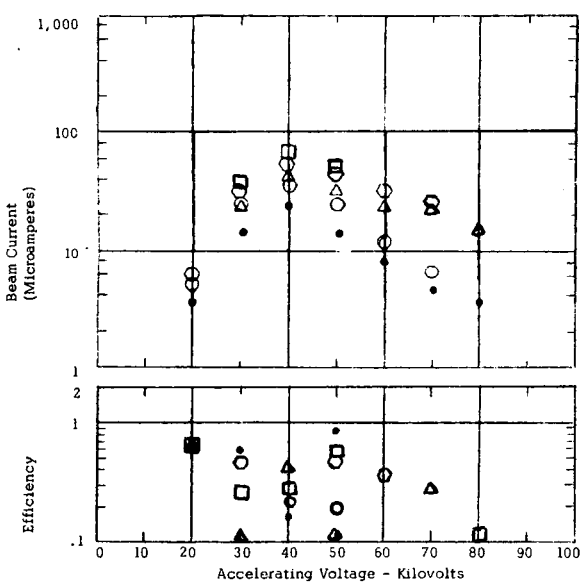

Figure 19. $\dot{M}$ = .25 mg/sec.

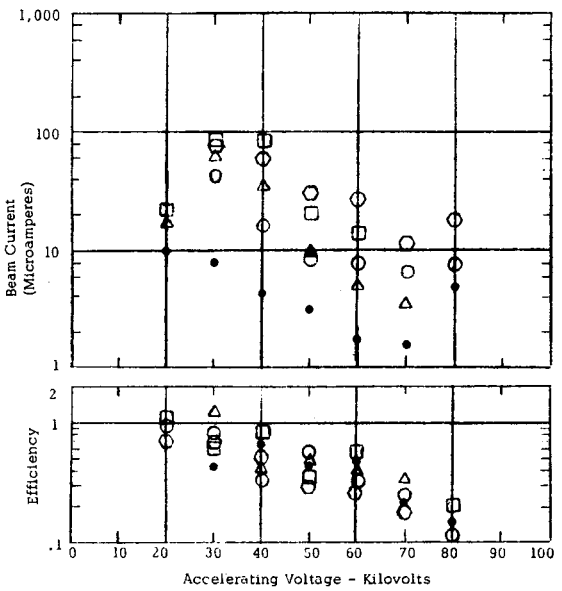

Figure 20. $\dot{M}$ = 1 mg/sec.

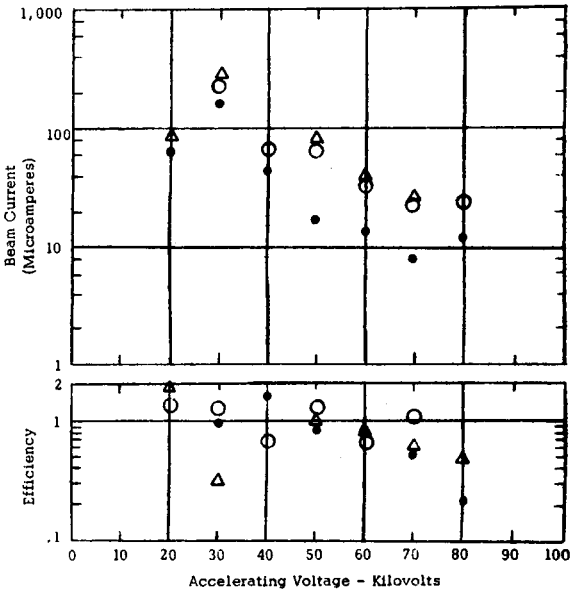

Figure 21. $\dot{M}$ = 7.5 mg/sec.

Beam Current and Efficiency as a Function of Voltage.
ω = 1,000 rpm

Order of Tests: •, ○, △, ⬡, □

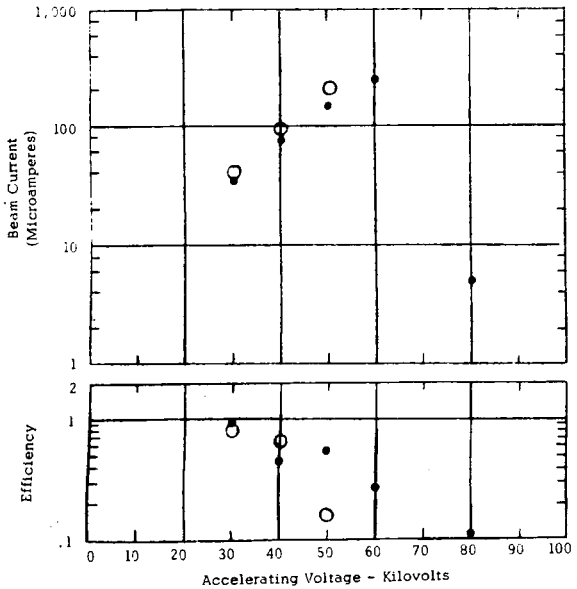

Figure 22. $\dot{M}$ = .25 mg/sec.

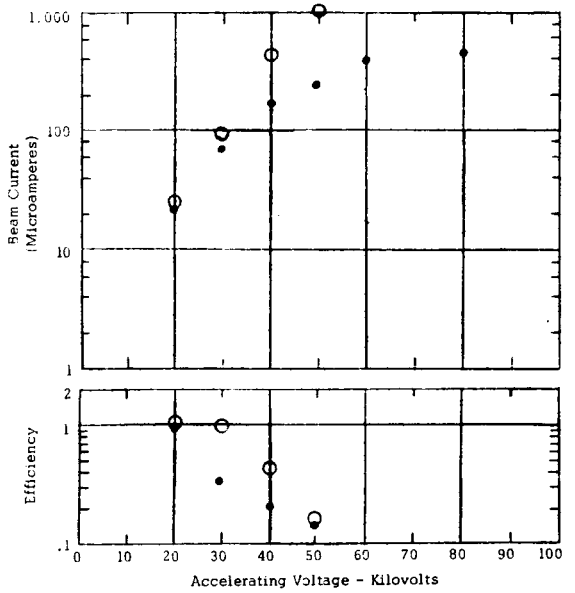

Figure 23. $\dot{M}$ = 1 mg/sec.

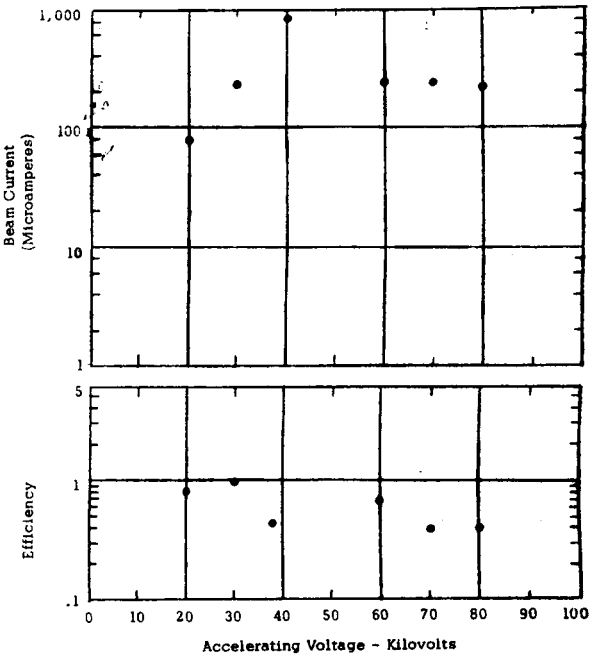

Figure 24. $\dot{M}$ = 7.5 mg/sec.

Beam Current and Efficiency as a Function of Voltage.
ω = 4,000 rpm

Order of Tests: ●, ○

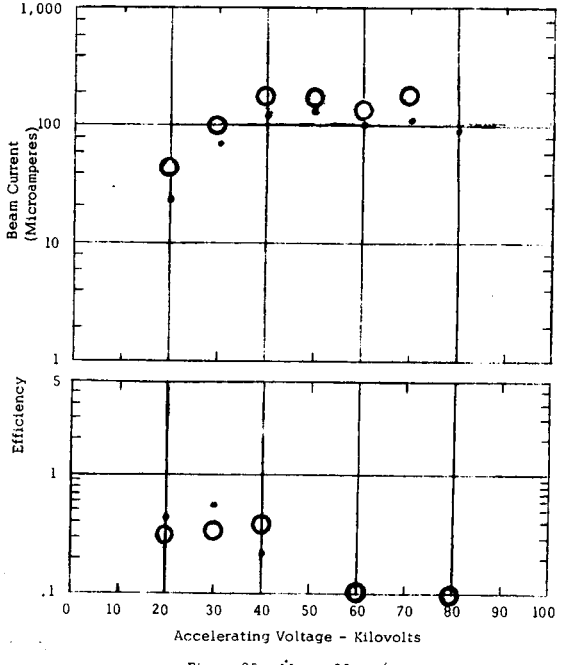

Figure 25. $\dot{M}$ = .25 mg/sec.

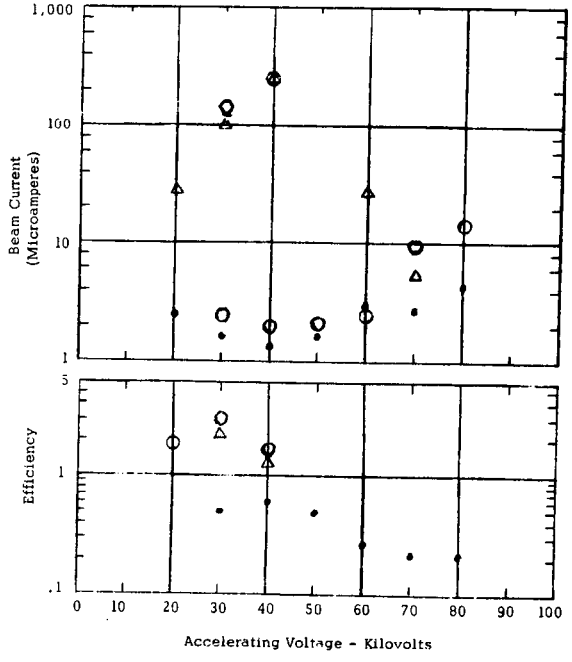

Figure 26. $\dot{M}$ = 1 mg/sec.

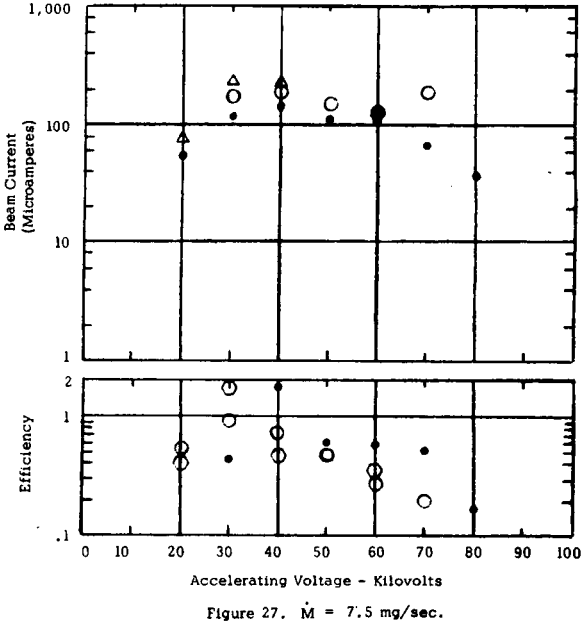

Figure 27. $\dot{M}$ = 7.5 mg/sec.

Beam Current and Efficiency as a Function of Voltage.
ω = 10,000 rpm

Order of Tests: ●, ○, △, ⬡

2) The efficiency eventually decreases with increasing voltage. This trend had been observed earlier with other propellants, in particular, with glycerol.

3) In each test, while the mass flow and the nozzle rotating speed was held constant, between 3 and 5 curves were obtained; each one during a time span of about 10 minutes. It can be seen that the beam current is higher in the later tests. This variation in beam current is probably attributable to the increase in temperature at the edge of the nozzle. It was not possible to monitor the temperature at the edge of the nozzle during a test. However, an observation can be made of a test run with an insulating nozzle which eventually softened to the point of being damaged (Figure 5). Such softening would indicate a minimum temperature of 120^{o} Centigrade.

The observations accomplished during normal operation, i.e., with the presence of a faint glow, are very similar to those of Maitland (Reference 12). In particular, a pressure rise of about 50% was noted by Maitland during his experiments. The same phenomenon was observed during the experiments described here.

It is important at this point to realize the dependency of the results obtained on the vacuum chamber utilized and on the pumping system. In particular, a possible explanation for the decrease in current above a certain value of the accelerating voltage may be as follows: At the high values of voltage (above 50 kilovolts) the pressure increases in the space between the nozzle and the collector so as to actually hinder the charging mechanism. With the lower vacuum pumping rates, the increase in pressure could not be contained in the space immediately adjacent to the nozzle and resulted in discharges throughout the entire vacuum chamber.

7. INTERPRETATION OF PERFORMANCE MAPPING EXPERIMENTS

The series of performance mapping experiments described above was intended to provide not only systematic performance data, but also a check on the theoretical results presented in Section 5 above. This theory postulates a beam of droplets with a homogeneous charge-to-mass ratio, whereas the actual experimental beam contains, in general both droplets of varied but relatively low charge-to-mass ratio (less than 10^4 coulombs/kilogram, say) and also ions with relatively high charge-to-mass ratio (above 10^4 coulombs/kilogram). Therefore, before comparing theory and data, it is necessary to smooth the data to extract an "equivalent" colloid beam for which the theory may conceivably be applicable. It is readily demonstrated that the current and thrust of this equivalent beam must be taken as:

$$I_{eq} = \frac{I_{low}}{\eta_{low}} \tag{1}$$

$$F_{eq} = \frac{F_{low}}{\eta_{low}} \tag{2}$$

where I_{low}, F_{low}, $\dot{m}_{low}$ are the total current, thrust, and mass flow, respectively, due to all particles of relatively low charge-to-mass ratio and

$$\eta_{low} \equiv \frac{F_{low}^2}{2\,V I_{low}\,\dot{m}_{low}} \tag{3}$$

Moreover, for low ion mass flows, it is readily seen that the total measured efficiency is given by

$$\eta_{meas} = \frac{I_{low}}{I_{meas}}\ \eta_{low} \tag{4}$$

where the subscript "meas" denotes a measured quantity produced by all particles of both low and high charge-to-mass ratio. Since virtually all the thrust is produced by the heavy particles, it follows that

$$I_{eq} = \left(\frac{I_{low}}{I_{meas}}\right)^2 \frac{I_{meas}}{\eta_{meas}} \tag{5}$$

$$F_{eq} = \left(\frac{I_{low}}{I_{meas}}\right) \frac{I_{meas}}{\eta_{meas}} \tag{6}$$

In analyzing a previous performance mapping experiment (Reference 4), we took

$$\frac{I_{low}}{I_{meas}} \simeq 1 \tag{7}$$

This was justified by the facts that, throughout the experiments, the measured total efficiency remained of order 1 and exhibited no systematic variation with mass flow, rotating speed, or voltage. However, one of the most striking regularities of the performance mapping experiment reported herein is the systematic and pronounced decrease in measured efficiency with increasing voltage. This fact implies that the ratio (I_{low}/I_{meas}) is also varying markedly. However, since data for estimating this variation quantitatively are unavailable, we cannot extract the equivalent colloid beam via (5) and (6). Thus, it is infeasible to employ the data systematically as a meaningful check on the theoretical results.

We have shown that, in general, it is invalid to smooth the present performance mapping data as we had legitimately and successfully smoothed the earlier data, i.e., by taking

$$I_{eq} = I_{meas}/\eta_{meas} \tag{8}$$

$$F_{eq} = F_{meas}/\eta_{meas} \tag{9}$$

Nevertheless, this smoothing may be meaningful for some ranges of operating parameters. Figures 28 through 31 were obtained in this fashion. Figures 28 and 29 show current and thrust data for a fixed mass flow and rotating speed and varying voltage; as before (reference 4), the current and thrust data are well-matched by V^3 and V^2 laws, respectively. Similarly, Figure 30 and 31 show the variation of thrust and current with mass flow for a fixed voltage and several rotating speeds; as before (Reference 4), the thrust and current appear to be independent of rotating speed and to vary linearly with mass flow. Thus, the data shown in Figures 28 through 31 are consistent with operation in the weak space-charge limit of the disintegration mode. This is generally true of the "partially smoothed" data from the present performance mapping experiment - insofar as these data are consistent with any of the limiting cases of the theory, they agree with the weak space-charge limit of the disintegration mode. In looking for such agreements, we have ignored the temperature dependence of propellant properties, though we recognize that this effect may be significant at the higher voltages and may improve the agreement.

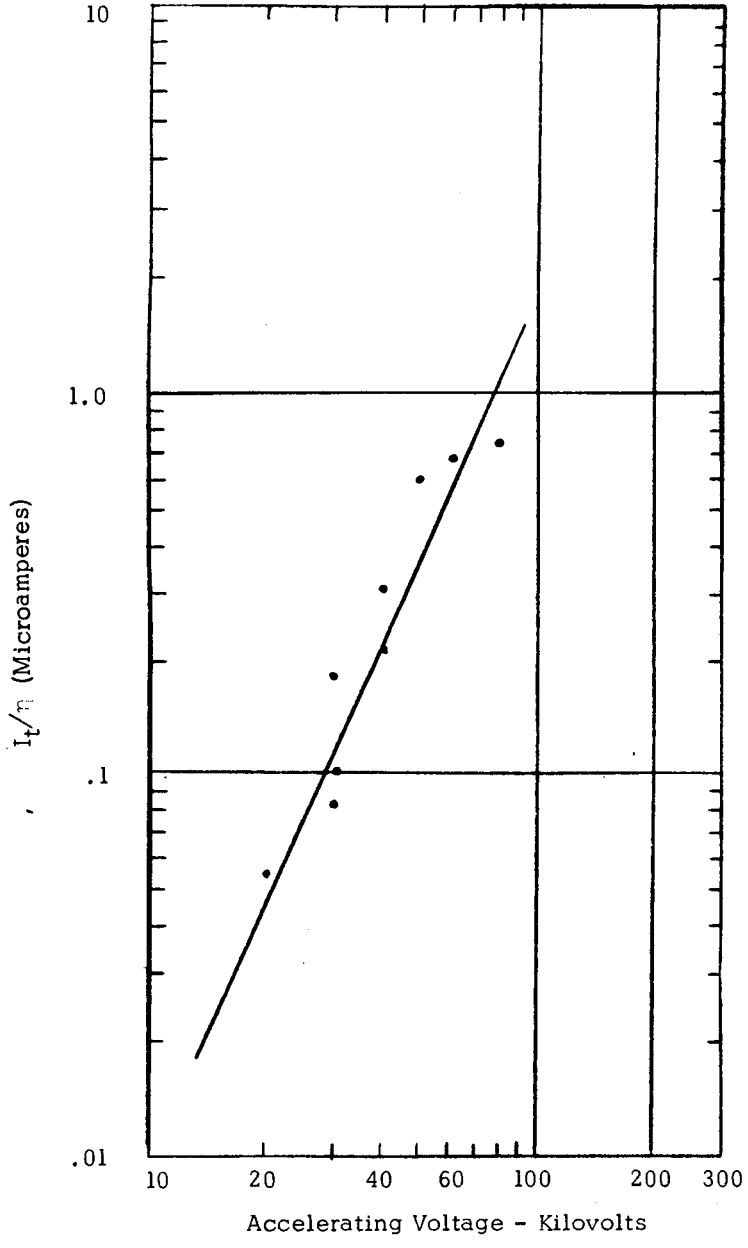

Figure 29. Equivalent Target Thrust vs Voltage for a Rotating Speed of 4,000 rpm and a Total Mass Flow Rate of 1×10^{-6} kg/sec.

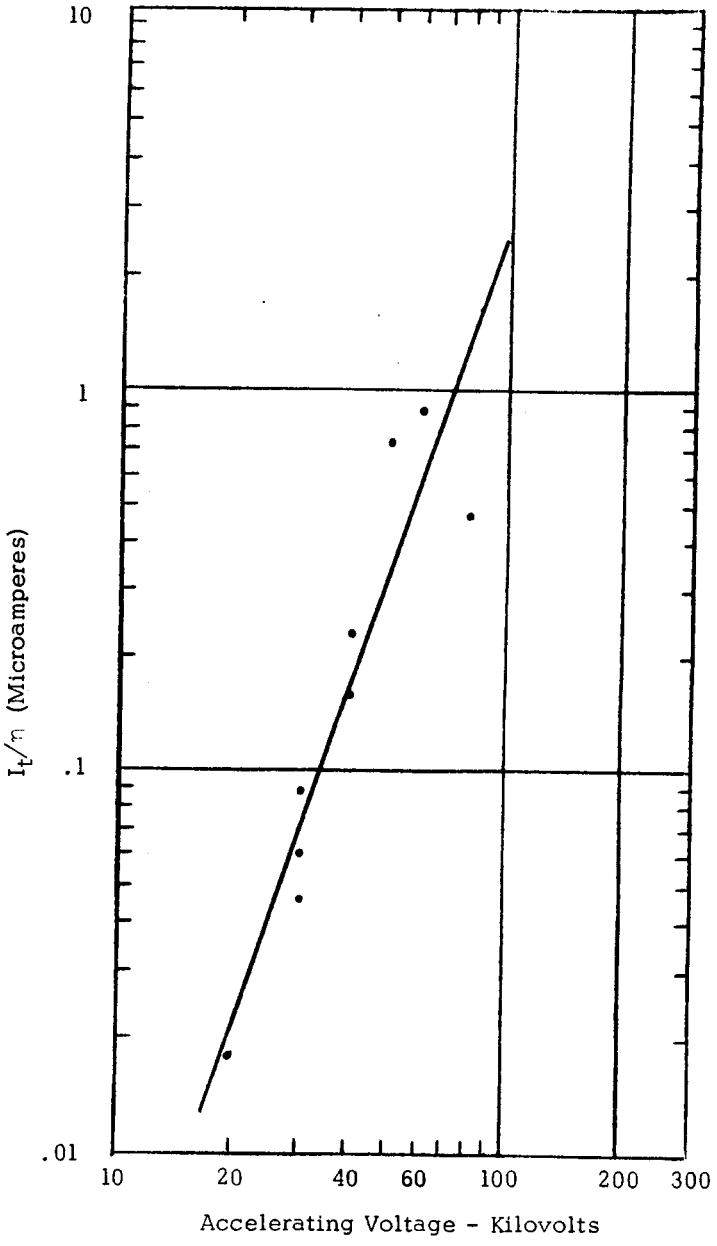

Figure 28. Equivalent Target Current vs Voltage for a Rotating Speed of 4,000 rpm and a Total Mass Flow Rate of 1×10^{-6} kg/sec.

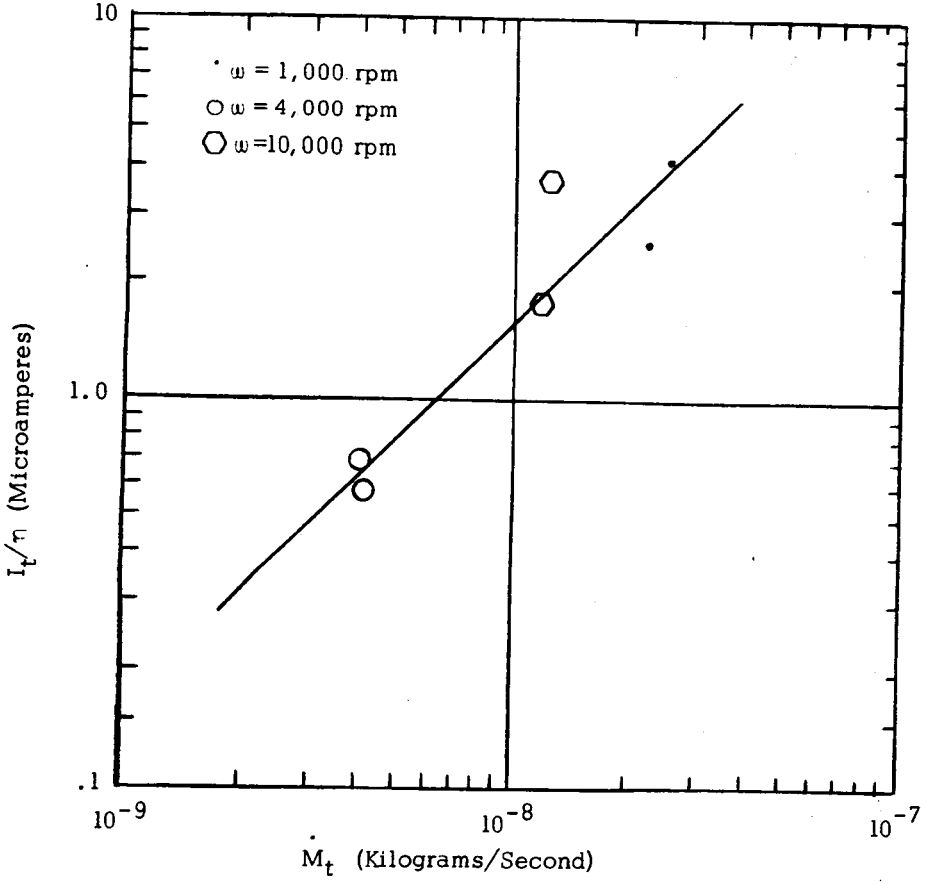

Figure 30. Equivalent Target Current vs Target Mass Flow Rate for a Voltage of 20 kv and Rotating Speeds of 1,000, 4,000 and 10,000 rpm.

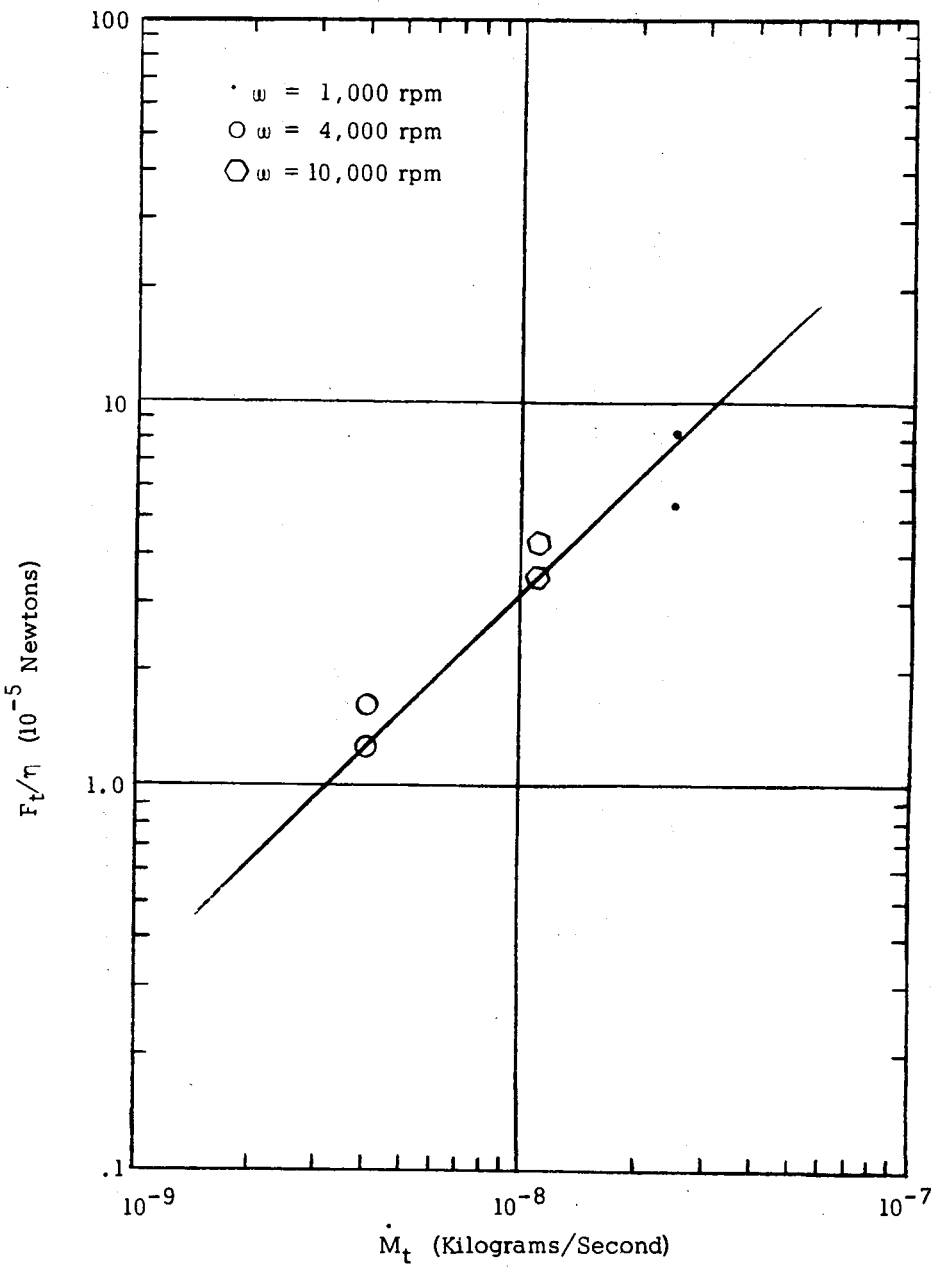

Figure 31. Equivalent Target Thrust vs Target Mass Flow Rate for a Voltage of 30 kv and Rotating Speeds of 1,000, 4,000 and 10,000 rpm.

REFERENCES

1. Carl T. Norgren, "Onboard Colloidal Particle Generator for Electrostatic Engines", Electric Propulsion Development, Progress in Astronautics and Aeronautics, Vol. 9 (New York Academic Press).

2. D. Gignoux, H.F. Anton, and H. Einbinder, "Nozzle for Colloidal Propulsion, Analytical Investigation", Final Report NASr-45, August 1961.

3. D. Gignoux, H.F. Anton, and J.J. Shea, "Charged Colloid Generating System for Electric Propulsion", NASA CR-54049, October 1963.

4. D. Gignoux, H.F. Anton, and J.J. Shea, "Development of a Charged Colloid Source for Electrostatic Propulsion", NASA CR-54176, October 1964.

5. E. Cohen, "Research on Charged Colloid Generation", APL TDR 64-75, June 1964.

6. D. Gignoux, "Electrostatic Generators in Space Power Systems", AIAA Paper No. 64-450, 1st AIAA Annual Meeting, Washington, D. C., June 1964.

7. I. E. Dayton, F. C. Shoemaker, and R. F. Mozley, Rev. Sci. Inst. 25, 485 (1954).

8. E. Mathieu, "Memoire sur le Mouvement Vibratoire d'une Membrane de Forme Elliptique", Journal de Math Puves et Appliques 13, 137, 1868.

9. N. W. McLachlan, "Theory and Application of Mathieu Functions", Clarendon Press, Oxford, pp. 40 and 98.

10. W. Paul and M. Raether, "Das Elektrische Massenfilter", Zeitschrift für Physik, Bd. 140, S. 262-273 (1955).

11. W. Paul, H. P. Reinhard and U. von Zahn, "Das Elektrische Massenfilter als Massenspektrometer und Isotopentrenner", Zeitschrift für Physik, Bd. 152, S. 143-182 (1958).

12. A. Maitland, "A Study of Glow Discharges Between Plane Electrodes at Pressures in the Range 10^{-6} - 10^{-4} Torr", Proceedings, International Symposium on Insulation of High Voltages in Vacuum, October 19 - 21, 1964, p.135.

ACKNOWLEDGEMENTS

The support of NASA - Lewis Research Center is gratefully acknowledged. This company wishes to thank Mssrs. J. Ferrante, D. Lockwood and J. H. Childs, whose guidance and many helpful suggestions have been most beneficial for the successful completion of this program.

ABSTRACT

A charged liquid colloid source has been built, which uses an intense electric field on the edge of a spinning nozzle. Experiments have been run with several organic propellants and liquid metals. Instrumentation has been built which has made possible the measurements of current, thrust, efficiency and the estimation of a charge-to-mass ratio distribution. A theoretical analysis of charging mechanism and of beam behavior, including space-charge effect has been accomplished.

FINAL REPORT DISTRIBUTION LIST

CONTRACT NAS3-6268

	Addressee	Number of Copies
1.	NASA Headquarters FOB - 10B 600 Independence Avenue, N. E. Washington, D. C. 20546 Attention: RNT/James Lazar	2
2.	NASA - Lewis Research Center Spacecraft Technology Division 21000 Brookpark Road Cleveland, Ohio 44135 Attention: J. H. Childs	2
3.	NASA - Lewis Research Center Spacecraft Technology Division 21000 Brookpark Road Cleveland, Ohio 44135 Attention: J. Ferrante	5
4.	NASA - Lewis Research Center Spacecraft Technology Procurement Section 21000 Brookpark Road Cleveland, Ohio 44135 Attention: John H. DeFord	1
5.	NASA - Lewis Research Center 21000 Brookpark Road Cleveland, Ohio 44135 Attention: Technology Utilization Office	1
6.	NASA - Lewis Research Center 21000 Brookpark Road Cleveland, Ohio 44135 Attention: Reports Control Office	1
7.	NASA - Lewis Research Center 21000 Brookpark Road Cleveland, Ohio 44135 Attention: Library	2

	Addressee	Number of Copies
8.	NASA - Lewis Research Center 21000 Brookpark Road Cleveland, Ohio 44135 Attention: C. T. Norgren	2
9.	NASA - Lewis Research Center 21000 Brookpark Road Cleveland, Ohio 44135 Attention: Edward A. Rickley, M.S. 301-1	1
10.	NASA - Lewis Research Center 21000 Brookpark Road Cleveland, Ohio 44135 Attention: H. R. Kaufmann, M.S. 301-1	1
11.	Commander Aeronautical Systems Division Wright-Patterson Air Force Base, Ohio Attention: AFAPL (APIE)/Mr. Robert Supp	1
12.	Commander Aeronautical Systems Division Wright-Patterson Air Force Base, Ohio Attention: AFAPL (APIE)/Mr. R. Hunter	1
13.	NASA - Marshall Space Flight Center Huntsville, Alabama Attention: (M-RP-DIR)/E. Stuhlinger	1
14.	NASA Scientific and Technical Information Facility Box 5700 Bethesda 14, Maryland Attention: RQT-2448/NASA Representative	6
15.	Rocketdyne Division of North American Aviation, Inc. Electric Propulsion Section Canoga Park, California Attention: Dr. J. F. Hon	1
16.	Rocket Power, Inc. 3016 East Foothill Boulevard Pasadena, California Attention: Dr. S. Singer	1

	Addressee	Number of Copies
17.	Ion Physics Corporation Burlington, Massachusetts Attention: Dr. Sam Nablo	1
18.	Astrosystems, Inc. 82 Naylon Avenue Livingston, New Jersey Attention: Mr. R. E. Weith, Jr.	1
19.	TRW Inc. Physical Research Laboratories 8433 Fallbrook Avenue Canoga Park, California Attention: Dr. D. B. Langmuir	1
20.	Reaction Motors Division Thiokol Chemical Corporation Denville, New Jersey Attention: Dr. Wilby Courtney	1
21.	Aerojet-General Nucleonics P. O. Box 77 San Ramon, California Attention: Dr. John Luce	1
22.	Gruman Aircraft Engineering Corporation Bethpage, Long Island, New York Attention: Mr. Paul Grinoch	1
23.	Hughes Research Laboratories 2011 Malibu Canyon Road Malibu, California Attention: Dr. Ron Knechtli	1
24.	Electro-Optical Systems, Inc. 300 North Halstead Street Pasadena, California Attention: Dr. A. T. Forrester	1
25.	The Martin Company P. O. Box 5837 Orlando, Florida 32808 Attention: Engineering Library MP 30	1

	Addressee	Number of Copies
26.	AFWL Kirtland Air Force Base, New Mexico Attention: WLPC/Capt. C. F. Ellis	1
27.	Aerospace Corporation P. O. Box 95085 Los Angeles, California 90045 Attention: Library Technical Document Group	1
28.	Westinghouse Astronuclear Laboratories Pittsburgh, Pennsylvania 15234 Attention: H. W. Szymanowski, Manager Electrical Propulsion Laboratory	1